

Simulating Floquet scrambling circuits on trapped-ion quantum computers

Kazuhiro Seki,^{1,*} Yuta Kikuchi,^{2,3,†} Tomoya Hayata,^{4,3,‡} and Seiji Yunoki^{1,5,6,7,§}

¹Quantum Computational Science Research Team, RIKEN Center for Quantum Computing (RQC), Saitama 351-0198, Japan

²Quantinuum K.K., Otemachi Financial City Grand Cube 3F, 1-9-2 Otemachi, Chiyoda-ku, Tokyo, Japan

³Interdisciplinary Theoretical and Mathematical Sciences Program (iTHEMS), RIKEN, Wako, Saitama 351-0198, Japan

⁴Departments of Physics, Keio University School of Medicine, 4-1-1 Hiyoshi, Kanagawa 223-8521, Japan

⁵Computational Quantum Matter Research Team, RIKEN Center for Emergent Matter Science (CEMS), Wako, Saitama 351-0198, Japan

⁶Computational Materials Science Research Team, RIKEN Center for Computational Science (R-CCS), Kobe, Hyogo 650-0047, Japan

⁷Computational Condensed Matter Physics Laboratory,

RIKEN Cluster for Pioneering Research (CPR), Saitama 351-0198, Japan

(Dated: April 15, 2025)

Complex quantum many-body dynamics spread initially localized quantum information across the entire system. Information scrambling refers to such a process, whose simulation is one of the promising applications of quantum computing. We demonstrate the Hayden-Preskill recovery protocol and the interferometric protocol for calculating out-of-time-ordered correlators to study the scrambling property of a one-dimensional kicked-Ising model on 20-qubit trapped-ion quantum processors. The simulated quantum circuits have a geometrically local structure that exhibits the ballistic growth of entanglement, resulting in the circuit depth being linear in the number of qubits for the entire state to be scrambled. We experimentally confirm the growth of signals in the Hayden-Preskill recovery protocol and the decay of out-of-time-ordered correlators at late times. As an application of the created scrambling circuits, we also experimentally demonstrate the calculation of the microcanonical expectation values of local operators adopting the idea of thermal pure quantum states. Our experiments are made possible by extensively utilizing one of the highest-fidelity quantum processors currently available and, thus, should be considered as a benchmark for the current status of the most advanced quantum computers.

I. INTRODUCTION

The spreading or scrambling of quantum information is a characteristic feature of complex quantum many-body dynamics. Understanding the properties of information scrambling is crucial for addressing fundamental problems in quantum mechanics, including thermalization and chaos. As a quantum state evolves under unitary dynamics, it gradually loses microscopic details, ultimately retaining only macroscopic information, a process known as thermalization. As the system further evolves, quantum information is scrambled in the sense that initially localized information spreads, making it increasingly harder to recover from local measurements of the evolved state. The difficulty of information retrieval is closely tied to the complexity of quantum dynamics. For instance, it is intuitive to understand that information thrown into a fast scrambler, such as a black hole, would be highly challenging to recover. Indeed, the information scrambling was initially investigated to elucidate the complex black hole dynamics [1–5], and it is nowadays used to diagnose nonequilibrium properties of quantum many-body dynamics [6–9]. Extensive studies have been devoted to quantifying the information scrambling and understanding its quantum information-theoretic aspects by computing various indicators, including spectral form factors [10–13], Loschmidt echo [14–16], and out-of-time-ordered correlators (OTOCs) [3, 6, 9, 17–19].

Along with advances in analytical and numerical techniques for studying scrambling quantum dynamics, quantum computing has emerged as a promising tool for efficiently simulating such systems. Despite such anticipation and rapid developments of quantum processors, the full potential of quantum computing remains unrealized largely because of errors caused by interaction with environments and imperfect control of quantum operations. Extracting signals from currently available quantum hardware requires precise error characterization for each hardware. Furthermore, the way that errors affect the final outcome depends not only on the hardware but also heavily on the type of algorithm or quantum circuits employed, even when the same device is used. To realize large-scale quantum simulation of complex scrambling dynamics, which is one of the promising applications of quantum computing, it is crucial to assess the feasibility of proposed quantum algorithms on current hardware. Such assessments are essential for accurately estimating the computational resources required to scale up the system size.

In this study, we explore information scrambling of periodically driven (Floquet) systems by taking the kicked-Ising model as an example [20, 21]. In the context of non-equilibrium physics, the model is known to exhibit Floquet heating, a phenomenon where a quantum system is heated to the infinite temperature after evolution under periodic driving [22–27]. To assess the protocols characterizing and utilizing this heating phenomenon, we carry out three experiments fully exploiting the highest-fidelity trapped-ion quantum processors [28]. The present studies demonstrate the capability of currently available quantum devices for studying quantum dynamics, and pave the way to scale up experiments and potentially reach the realm of classically intractable system sizes

* kazuhiro.seki@riken.jp

† yuta.kikuchi@quantinuum.com

‡ hayata@keio.jp

§ yunoki@riken.jp

and evolution times.

In the first experiment, we employ the Hayden-Preskill recovery (HPR) protocol [1, 29, 30]. So far, HPR protocols [31, 32] and teleportation protocols inspired by gravitational theory [33, 34] have been demonstrated on other programmable quantum devices. Here, to fully explore the information scrambling of the Floquet circuits, we conduct the protocol across all the time steps until late-time scrambling behavior is confirmed. The raw experimental results clearly show the growth of HPR signals at late times, indicating the scrambling of information as theoretically anticipated. Moreover, assuming a simple noise model [30, 35, 36], we mitigate the noise effect and demonstrate that the error-mitigated results better agree with the exact results obtained by classical simulations.

In the second experiment, we perform the interferometric protocol for calculating OTOCs [8, 37]. We note that several experimental efforts have been devoted to calculating OTOCs [38–42]. We address spatial and temporal dependence of the OTOCs executing the circuits involving a maximum of 367 entangling gates causally connected to the final measurements. The results indicate that information scrambling grows ballistically during the Floquet dynamics at a chosen set of kicked-Ising parameters, which is clearly seen after applying the error mitigation [8, 41]. While the OTOCs and the HPR signals are closely related and carry similar information, there are some pragmatic differences in experiments: the HPR protocol uses two copies of the original system by using almost twice as many qubits as the interferometric protocol, although it is robust against decoherence [30, 35, 36].

In the third experiment, we calculate the thermal expectation values of a local operator as an application of the scrambling circuits. In statistical mechanics, ensembles are represented by probabilistic mixtures of a macroscopically large number of eigenstates of a Hamiltonian. Randomized protocols have been developed to recover such thermal properties using randomly sampled pure states, including thermal pure quantum (TPQ) states for microcanonical and canonical ensembles [43–51]. To make use of the TPQ states in quantum algorithms, unitary or state designs play key roles in preparing relevant random states efficiently on quantum computers [52–57].

Giving the implications of the first two experimental observations, which suggest the states evolved under chaotic dynamics approximate a state 2-design [58–61],¹ we proceed to calculate the expectation value of local operators with respect to the microcanonical ensemble by employing the scrambling circuits as a subroutine. However, it should be noted that, from the viewpoint of gate complexity, use of our Floquet scrambling circuits instead of, e.g., the Clifford scrambler does not offer significant advantages on devices featuring native long-range gate operations such as trapped-ion devices. Nevertheless, our protocol should be favored on hardware with limited connectivity because the evolution operator of

the kicked-Ising model does not require long-range entangling gates.

The rest of this paper is organized as follows. In Sec. II, we provide a brief review of the kicked-Ising model as a periodically driven quantum system. In Sec. III, we discuss the quantum algorithms, which we will demonstrate using the trapped-ion quantum computers. We introduce the HPR protocol and interferometric protocol for OTOCs, both of which serve as measures of information scrambling. Additionally, we describe a method for computing thermal expectation values based on the concept of TPQ states using the scrambling circuits. The experimental setups and results obtained are presented in Sec. IV. Finally, we provide conclusions and outlooks in Sec. V. In Appendix A, the noise model we adopted to mitigate the hardware noise in the experiments is explained. Appendix B provides classical numerical results of OTOCs to supplement the experimental results presented in Sec. IV. The rest of the appendices are devoted to elaborating the computation of thermal expectation values using scrambling circuits. We numerically justify the use of scrambling circuits to estimate the normalized trace in Appendix C. In Appendix D, we carefully study the error in microcanonical TPQ expectation values. The asymptotic resource analysis for the imaginary time evolution algorithm used in the present experiments is found in Appendix E. Finally, we provide additional experimental results of thermal expectation values in Appendix F.

II. KICKED-ISING MODEL AS A FLOQUET CIRCUIT

Floquet evolution is described by a time-dependent Hamiltonian periodic in time, $H(t) = H(t + T)$, with the period T . Due to the periodic driving, the system does not conserve energy. Furthermore, such periodically driven nonintegrable systems are expected to eventually heat up to infinite temperature by acquiring energy from the driving force, known as the Floquet heating, occurring after an exponentially long time in their driving frequency [22, 23, 25–27]. A notable example is a Hamiltonian dynamics approximated by the first-order product (Lie-Trotter) formula [62],

$$\left(\prod_{i=1}^K e^{-iH_i \frac{T}{K}} \right)^{mK}, \quad (1)$$

for a static Hamiltonian $H = \sum_{i=1}^K H_i$ (H_i are non-commutative with each other) and total evolution time mT with an integer m . This can be considered as the periodically driven dynamics with the driving period T over m cycles. It has been observed that, in the Trotter time evolution of an Ising spin chain, there exists a transition or crossover between many-body localized and quantum chaotic regimes as a function of the driving period T , or equivalently the inverse driving frequency, characterized by the inverse participation ratio and OTOCs [63–65].

In this study, we consider the kicked-Ising model on a one-dimensional chain, which is a periodically driven quantum system described by the following time-dependent Hamilto-

¹ We consider an ensemble of states evolved under a Floquet dynamics, instead of a Hamiltonian dynamics [58].

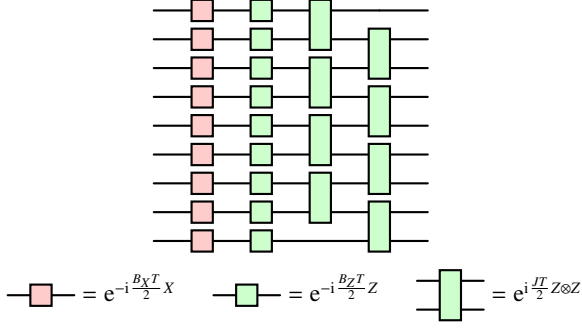


FIG. 1. The circuit representation of a single Floquet circle described by the Floquet operator U_F in Eq. (3) for a one-dimensional system consisting of $N = 9$ qubits under open boundary conditions.

nian:

$$H(t) = \begin{cases} H_X = B_X \sum_{i=1}^N X_i, & t \in [0, T/2), \\ H_Z = -J \sum_{i=1}^{N \text{ or } N-1} Z_i Z_{i+1} + B_Z \sum_{i=1}^N Z_i, & t \in [T/2, T), \end{cases} \quad (2)$$

where X_i (Z_i) is the x (z) component of the Pauli operators at site i , and N is the total number of sites. We will consider both open and periodic boundary conditions and accordingly the sum of Ising-coupling terms in H_Z is properly chosen. When the periodic boundary conditions are imposed, the $N + 1$ th site is identified with the 1st site. The corresponding time evolution over a single period is described by the Floquet operator,

$$U_F = e^{-iH_Z T/2} e^{-iH_X T/2}, \quad (3)$$

which consists of $O(N)$ single-qubit gates and two-qubit gates. An example of the circuit representation of U_F is shown in Fig. 1. Depending on the model parameters, connectivity of the Ising-coupling terms, and initial states, this model may transiently exhibit discrete-time quasicrystalline orders before thermalization [66]. In our experiments, however, we focus mainly on simulating the model with the parameters at and around the self-dual point $|JT| = |B_X T| = \pi/2$, where the dynamics is maximally chaotic [67–70].

III. METHODS

We utilize the HPR fidelity and OTOCs as indicators of information scrambling and introduce two protocols for calculating these quantities. Furthermore, we discuss the calculation of thermal expectation values as an application of scrambling circuits. Those three protocols are implemented on quantum hardware, as detailed in Section IV.

A. Hayden-Preskill recovery (HPR) protocol

The HPR protocol provides a means to characterize the scrambling properties of unitary dynamics [1, 29, 30]. This protocol can be understood as the teleportation of an input quantum state from a local subsystem A to a distant subsystem R' (see Fig. 2). Remarkably, the degree of scrambling in the dynamics is directly correlated with the teleportation fidelity. Specifically, more scrambling dynamics lead to higher teleportation fidelity, as elucidated further below.

For illustrative purposes, we first explain the top circuit in Fig. 2. Let us denote the number of qubits in subsystem A as N_A with the dimension of the corresponding Hilbert space \mathcal{H}_A being $d_A = 2^{N_A}$, and similarly for other subsystems. The sizes of the subsystem satisfy $N_A = N_{A'} = N_R = N_{R'}$, $N_B = N_{B'}$, $N_C = N_{C'}$, $N_D = N_{D'}$, and $N_A + N_B = N_C + N_D = N$. The circuit starts with the state $|\psi\rangle_A \otimes |\text{EPR}\rangle_{BB'} \otimes |\text{EPR}\rangle_{R'A'}$, where $|\psi\rangle$ is the state to be teleported and the EPR states are defined as $|\text{EPR}\rangle_{BB'} := d_B^{-1/2} \sum_{i=1}^{d_B} |i\rangle_B \otimes |i\rangle_{B'}$ and $|\text{EPR}\rangle_{R'A'} := d_A^{-1/2} \sum_{i=1}^{d_A} |i\rangle_{R'} \otimes |i\rangle_{A'}$. After applying $U_{AB} \otimes U_{A'B'}$ with U_{AB} ($U_{A'B'}$) being a unitary evolution: $\mathcal{H}_A \otimes \mathcal{H}_B \rightarrow \mathcal{H}_C \otimes \mathcal{H}_D$ (the corresponding backward evolution: $\mathcal{H}_{A'} \otimes \mathcal{H}_{B'} \rightarrow \mathcal{H}_{C'} \otimes \mathcal{H}_{D'}$), we measure the state on DD' and post-select only when it is projected onto $|\text{EPR}\rangle_{DD'}$. Upon the post-selection, we find the state $|\psi'\rangle$ as an output on R' , which is close to the input state $|\psi\rangle$ at late times, i.e. $\langle \psi' | \psi \rangle \sim 1$, if the unitary U has scrambled the input quantum state.

To extract the scrambling property of the unitary U , independent of the input state $|\psi\rangle$, we employ another protocol using the circuit at the bottom of Fig. 2, where $|\psi\rangle$ is replaced with another EPR state entangled with the reference state on R . The whole state before the measurement is given by

$$|\Phi\rangle := (U_{AB} \otimes U_{A'B'}) |\text{EPR}\rangle_{RA} \otimes |\text{EPR}\rangle_{BB'} \otimes |\text{EPR}\rangle_{R'A'}. \quad (4)$$

We apply the projector $\Pi_{DD'} := |\text{EPR}\rangle\langle\text{EPR}|_{DD'}$ by measuring the state on DD' and post-selecting, yielding

$$|\Psi\rangle := \frac{\Pi_{DD'} |\Phi\rangle}{\sqrt{P_{\text{EPR}}}}, \quad P_{\text{EPR}} := \text{Tr}[\Pi_{DD'} |\Phi\rangle\langle\Phi|], \quad (5)$$

where P_{EPR} is referred to as the post-selection probability. We then read off the probability that the state on RR' is in $|\text{EPR}\rangle_{RR'}$ as

$$F_{\text{EPR}} := \text{Tr}[\Pi_{RR'} |\Psi\rangle\langle\Psi|], \quad (6)$$

which quantifies how close the resultant state on R' is to the input state in terms of fidelity. The quantity F_{EPR} is known as the recovery fidelity.

B. Out-of-time-ordered correlators (OTOCs)

An OTOC quantifies the sensitivity of a given quantum dynamics U to the insertion of a butterfly operator O_D , measuring how O_D evolves under the time evolution U via a measurement operator O_A . The OTOC with respect to a density operator ρ is defined as

$$\text{OTOC}_\rho := \text{Tr}[\rho U^\dagger O_D^\dagger U O_A^\dagger U^\dagger O_D U O_A], \quad (7)$$

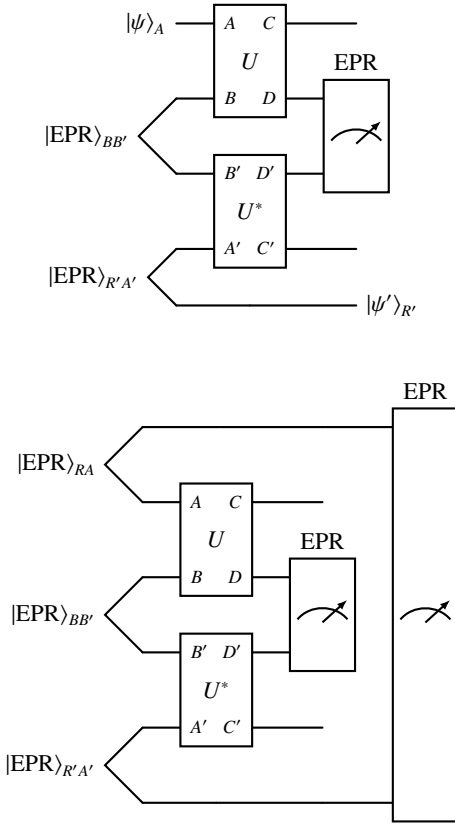


FIG. 2. The quantum circuits for the HPR protocol. (Top) The state $|\psi\rangle$ is approximately teleported to the bottom register on R' . (Bottom) The input state $|\psi\rangle$ is replaced by an EPR state entangled with a reference register on R to eliminate the state dependence.

where O_A and O_D are operators supported on subsystems A and D , respectively. Provided that the subsystems A and D are disjoint, the growth of operator $U^\dagger O_D U$ leads to the decay of the OTOC as it starts to overlap with O_A . For scrambling circuits, the OTOC decays exponentially in N at late times [9].

We employ the interferometric circuit shown in Fig. 3 to compute OTOCs [8, 37]. The circuit comprises the system register and a single-qubit ancillary register shown at the top of the figure, with the composite system initialized to $|+\rangle \langle +| \otimes \rho$. At the end of the circuit, the ancillary qubit is measured in the X basis to extract the values of the OTOCs. For OTOCs with complex values, the measurement in the X basis (Y basis) retrieves its real (imaginary) part.

We provide several remarks to make connections to the HPR protocol: Firstly, the post-selection probability P_{EPR} in the HPR protocol relates to a scrambling property through the operator-averaged OTOC as follows [29]:

$$\begin{aligned} P_{\text{EPR}} &= \mathbb{E}_{O_A \sim U(d_A), O_D \sim U(d_D)} [\text{OTOC}_{1/d}] \\ &= \frac{1}{d_A^2 d_D^2} \sum_{O_A \in \text{Pauli}_A} \sum_{O_D \in \text{Pauli}_D} \text{OTOC}_{1/d}, \end{aligned} \quad (8)$$

where the OTOCs are evaluated with respect to the maximally mixed state $\rho = I^{\otimes N}/d$ with $d = 2^N$ being the dimension of the Hilbert space. The Haar averages of O_A and O_D are taken

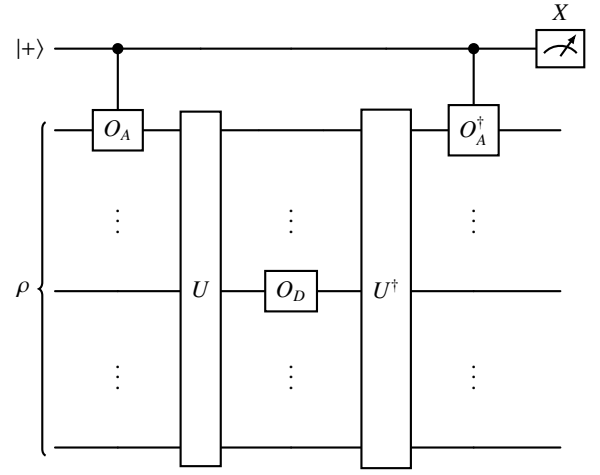


FIG. 3. The interferometric circuit employed to compute the OTOC defined in Eq. (7). The qubit at the top is the single-qubit ancillary register initialized to $|+\rangle$, while the remainder constitutes the system register with the input state ρ . At the end of the circuit, the ancillary qubit is measured in the X basis.

over the unitary operators supported on A and D , respectively, implying that the operator-averaged OTOC is independent of the choice of operators but still depends on the choice of the supports A and D . On the right-hand side, Pauli_A and Pauli_D denote the sets of all Pauli operators supported on A and D , respectively. In the second equality, we used the fact that the Haar average of the first moment of a unitary operator and its Hermitian conjugate can be replaced by the average over equally weighted Pauli operators.

Secondly, the recovery fidelity F_{EPR} is expressed as [29],

$$F_{\text{EPR}} = \frac{1}{d_A^2 P_{\text{EPR}}}. \quad (9)$$

In particular, when the operator U is a Haar random unitary operator, P_{EPR} takes the value $d_A^{-2} + d_D^{-2} - (d_A d_D)^{-2}$, resulting in the recovery fidelity being $4^{-\delta}$ -close to unity for $N_D > N_A + \delta$. More generally, the recovery fidelity F_{EPR} increases significantly at late times when U scrambles the input state, thereby serving as an indicator of scrambling similar to OTOCs.

Thirdly, the recovery fidelity F_{EPR} carries equivalent information to the operator-averaged OTOC in the absence of errors. However, the HPR protocol offers an advantage in the presence of hardware noise. In the HPR protocol, scrambling induces the growth of F_{EPR} , while decoherence causes the fidelity to decay [30]. This contrasts with OTOCs, which decay due to both scrambling and decoherence. Consequently, distinguishing between them becomes challenging in noisy simulations. In extreme cases, OTOCs may decay even in the absence of scrambling under strong decoherence.

Finally, the advantage of the interferometric protocol for OTOCs over the HPR protocol lies in its capability to handle larger system sizes. This becomes particularly crucial when the number of available qubits is limited.

C. Thermal expectation value from scrambling circuits

As an application of the scrambling circuits, we calculate the expectation value of a local operator O with respect to a microcanonical ensemble:

$$\langle O \rangle = \text{Tr}[O\rho_\sigma(E)], \quad \rho_\sigma(E) = \frac{e^{-(E-\mathcal{H})^2/2\sigma^2}}{\text{Tr}[e^{-(E-\mathcal{H})^2/2\sigma^2}]}, \quad (10)$$

where \mathcal{H} denotes the Hamiltonian of a thermal system, distinct from the Floquet Hamiltonian H in Eq. (2). Selecting the width parameter $\sigma \propto \sqrt{N}$ ensures that the expectation value converges to the correct microcanonical expectation value in the thermodynamic limit. Motivated by the idea of microcanonical TPQ states [49], we first consider a state k -design, defined as an ensemble \mathcal{E} of states reproducing the statistics of k -th moments of the Haar random distribution, i.e.,

$$\mathbb{E}_{|\psi\rangle \sim \mathcal{E}}[(|\psi\rangle\langle\psi|)^{\otimes k} O] = \mathbb{E}_{|\psi\rangle \sim \text{Haar}}[(|\psi\rangle\langle\psi|)^{\otimes k} O], \quad (11)$$

for any operator O . By sampling a pure state $|\psi\rangle$ randomly from a state 2-design, the estimated expectation value $\langle O \rangle$ in Eq. (10) is given as

$$\langle O \rangle^{(\text{est})} = \frac{\langle\psi| O e^{-(E-\mathcal{H})^2/2\sigma^2} |\psi\rangle}{\langle\psi| e^{-(E-\mathcal{H})^2/2\sigma^2} |\psi\rangle}. \quad (12)$$

For a pure state $|\psi\rangle$ sampled from a state k -design with $k \geq 2$,² the target expectation value is estimated with exponentially small variance in system size N . More precisely, the following inequality

$$\begin{aligned} & \Pr_{|\psi\rangle \sim 2\text{-design}}[|\langle O \rangle^{(\text{est})} - \langle O \rangle| \leq \epsilon] \\ & \geq 1 - \mathcal{O}(\sqrt{\text{Tr}[\rho_\sigma(E)^2]}/\epsilon^2) = 1 - \mathcal{O}(e^{-cN}/\epsilon^2), \end{aligned} \quad (13)$$

follows from the Chebyshev inequality for some positive constant c [49, 50]. Here, the left-hand side represents the probability that the estimator $\langle O \rangle^{(\text{est})}$ approximates $\langle O \rangle$ within an error of at most ϵ , considering a pure state $|\psi\rangle$ randomly sampled from a state 2-design.³ In the last equality, we used that the purity $\text{Tr}[\rho_\sigma(E)^2]$ decays exponentially, that is, the thermal entropy of $\rho_\sigma(E)$ follows a volume law, which holds for a typical state [49] (see Appendix D for details). Therefore, the inequality states that $\langle O \rangle^{(\text{est})}$ provides an ϵ -precise estimator with a probability exponentially close to 1. We prove this statement in Appendix D. Consequently, a single instance of a random state suffices when the associated purity of a targeted microcanonical state rapidly decays.

On the other hand, the quantum states generated after the scrambling time evolution approximate a state k -design [58–61]. Considering that the Floquet operator U_F exhibits scrambling properties, we expect that $(U_F)^m |\psi_0\rangle$ behaves as a state sampled from a state 2-design. In other words, the ensemble

$$\Psi = \{(U_F)^m |\psi_0\rangle \mid m \in \mathbb{N}\} \quad (14)$$

approximates a state 2-design if the evolution time mT exceeds the scrambling time. Supplementary numerical analyses supporting this assertion can be found in Appendix C.

Combining these two observations, we attempt to compute the microcanonical expectation value of O with the single state $|\psi\rangle = (U_F)^m |\psi_0\rangle$ [55, 71–76]. To implement $e^{-(E-\mathcal{H})^2/2\sigma^2}$, we rewrite the operator as follows:

$$\begin{aligned} e^{-(E-\mathcal{H})^2/2\sigma^2} &= \frac{\sigma}{\sqrt{2\pi}} \int_{-\infty}^{\infty} dt e^{-\sigma^2 t^2/2} e^{iEt} e^{-i\mathcal{H}t} \\ &\approx \frac{\sigma}{\sqrt{2\pi}} \sum_{s=-S}^S \Delta t e^{-\sigma^2 (s\Delta t)^2/2} e^{iEs\Delta t} e^{-i\mathcal{H}s\Delta t}, \end{aligned} \quad (15)$$

where the integral is discretized and the cutoff $S \in \mathbb{N}$ is introduced to truncate the infinite sum. Therefore, the task on the quantum processor boils down to evaluating the following amplitudes:

$$\mathcal{L}_O(s\Delta t) := \langle\psi_0| (U_F)^{\dagger m} O e^{-i\mathcal{H}s\Delta t} (U_F)^m |\psi_0\rangle, \quad (16)$$

and

$$\mathcal{L}(s\Delta t) := \langle\psi_0| (U_F)^{\dagger m} e^{-i\mathcal{H}s\Delta t} (U_F)^m |\psi_0\rangle, \quad (17)$$

for $s = -S, -S+1, \dots, S$. The quantity in Eq. (17) is known as Loschmidt amplitude [14–16]. We then perform classical post-processing of the outcomes of quantum computations using Eq. (15), i.e.,

$$D_O(E) := \frac{\sigma}{\sqrt{2\pi}} \sum_{s=-S}^S \Delta t e^{-\sigma^2 (s\Delta t)^2/2} e^{iEs\Delta t} \mathcal{L}_O(s\Delta t), \quad (18)$$

and

$$D(E) := \frac{\sigma}{\sqrt{2\pi}} \sum_{s=-S}^S \Delta t e^{-\sigma^2 (s\Delta t)^2/2} e^{iEs\Delta t} \mathcal{L}(s\Delta t). \quad (19)$$

Notice that $D(E)$ is the density of states of \mathcal{H} with respect to the energy E . Using these quantities, the microcanonical expectation value of O is estimated as

$$\langle O \rangle^{(\text{est})} = \frac{D_O(E)}{D(E)}. \quad (20)$$

Three remarks are in order. First, evaluating $\mathcal{L}_O(s\Delta t)$ and $\mathcal{L}(s\Delta t)$ to estimate the normalized traces $\text{Tr}[O e^{-i\mathcal{H}s\Delta t}]/2^N$ and $\text{Tr}[e^{-i\mathcal{H}s\Delta t}]/2^N$, respectively, with an additive error of $1/\text{poly}(N)$ can be hard tasks for classical computation. The potential hardness is based on the fact that the normalized trace estimation is a DQC1 complete problem, for which no polynomial-time classical algorithm is likely to exist [77–80].

² Similarly, a unitary k -design is an ensemble \mathcal{F} of unitary operators that reproduces the statistics of k -th moments of the Haar random distribution, i.e., $\mathbb{E}_{U \sim \mathcal{F}}[U^{\dagger \otimes k} O U^{\otimes k}] = \mathbb{E}_{U \sim \text{Haar}}[U^{\dagger \otimes k} O U^{\otimes k}]$ holds for any operator O .

³ A pure state $|\phi\rangle$ sampled from an ensemble Φ is called a microcanonical TPQ state if it satisfies the condition: $\Pr_{\phi \sim \Phi}[|\langle \phi | O_i | \phi \rangle - \langle O \rangle| \geq \epsilon] \leq \mathcal{O}(e^{-cN})$ for a predefined set of operators $\{O_i\}_i$. Therefore, $e^{-(E-\mathcal{H})^2/4\sigma^2} |\psi\rangle / \|e^{-(E-\mathcal{H})^2/4\sigma^2} |\psi\rangle\|$ with $|\psi\rangle$ sampled from a state 2-design is considered a microcanonical TPQ state.

See also Refs. [81, 82] for the normalized partition function problem with one-clean qubit. Second, the protocol presented here, nevertheless, requires a non-scalable shot overhead to evaluate the expectation value in Eq. (12) within a given uncertainty. This is because a scrambled state typically has a small overlap with the state $\rho_\sigma(E)$ in Eq. (10), particularly for small E (see Appendix E for details). We note that efforts have been made to reduce the overhead by classically sampling the input states to address the low-energy microcanonical states as well as the low-temperature canonical states [73–76]. Third, quadratic improvement of asymptotic runtime for calculating the expectation value in Eq. (12) can be achieved, for instance, by adopting the algorithm proposed in Ref. [72]. However, we employ the present protocol to experimentally demonstrate the property of scrambling circuits as an approximate state 2-design on a currently available noisy quantum device (see Appendix C for supplementary analyses).

IV. RESULTS

We experimentally demonstrate the aforementioned protocols on Quantinuum H1-1 and H1-2 trapped-ion quantum computers. The specifications of H1 quantum computers at the time of the experiments are as follows: both H1 quantum computers consist of 20 qubits, each qubit comprised of the $S_{1/2}$ hyperfine clock states of a trapped $^{171}\text{Yb}^+$ ion. The H1 systems natively implement single-qubit rotation gates and two-qubit gates $e^{-i\frac{\theta}{2}Z\otimes Z}$ parametrized by a real angle θ . All gate operations are performed in one of five gate zones, each operating in parallel. The two-qubit native gates can be applied to an arbitrary pair of qubits by shuttling ions to gate zones, thus realizing all-to-all connectivity. Average single- and two-qubit gate infidelities are about 0.004% and 0.2%, respectively. Specifically, the average infidelity of the native two-qubit gate, $e^{-i\frac{\theta}{2}Z\otimes Z}$, is currently characterized as

$$p_{2Q}(\theta) = p \left(p_a \frac{|\theta|}{\pi} + p_b \right), \quad (21)$$

with $p_a = 1.651$, $p_b = 0.175$, and $p = 1.38 \times 10^{-3}$ for the H1-1 system, and $p_a = 1.651$, $p_b = 0.175$, and $p = 2.97 \times 10^{-3}$ for the H1-2 system. State preparation and measurement errors are 0.3% on average. See Ref. [83] for more details. All the quantum circuits used in the experiments are compiled with TKET 1.24 for the native gate set of the Quantinuum H1 quantum computers at optimization level 2 [84].

A. Hayden-Preskill recovery protocol

Figure 4 shows the experimentally obtained post-selection probability $P_{\text{EPR}}^{(\text{noisy})}$ and recovery fidelity $F_{\text{EPR}}^{(\text{noisy})}$ as a function of the number of Floquet cycles m . The experiments are performed by executing the circuit shown in the bottom of Fig. 2 on the Quantinuum H1-1 system. We use two copies of the one-dimensional spin chain composed of $N = 9$ sites under open boundary conditions, with subsystems of $N_A = 1$ and

$N_D = 2$ sites each located on the opposite ends of the chain, thus utilizing a total of $2(N_R + N) = 20$ qubits. Exact results are obtained from classical simulations. The parameter T is set to two different values, $JT = 1.3$ and $\pi/2$, while the other parameters are fixed at $(B_X/J, B_Z/J) = (1, 1.3)$. Note that the circuit at $JT = 1.3$ is expected to be less scrambling than at the self-dual point $JT = \pi/2$. Comparison between the two allows us to study whether and how the error mitigation based on the depolarizing noise model works for scrambling and non-scrambling cases.

First of all, the qualitative agreement between the experimental raw data and the exact results firmly demonstrates the ability of the quantum computer to simulate quantum many-body dynamics involving unitary circuits and measurements. As shown in Figs. 4(c) and 4(d), the raw data of $F_{\text{EPR}}^{(\text{noisy})}$ agrees with the exact results within the statistical uncertainty, confirming the robustness of $F_{\text{EPR}}^{(\text{noisy})}$ against incoherent noise [30]. The discrepancy between the experimental and exact results for $P_{\text{EPR}}^{(\text{noisy})}$ in Figs. 4(a) and 4(b) shall be accounted for by considering the depolarizing noise below.

We perform error mitigation on $P_{\text{EPR}}^{(\text{noisy})}$ and $F_{\text{EPR}}^{(\text{noisy})}$ assuming the depolarizing noise model of the form in Refs. [30, 36]. As described in more details in Appendix A 1, the error-mitigated post-selection probability $P_{\text{EPR}}^{(\text{mit})}$ and recovery fidelity $F_{\text{EPR}}^{(\text{mit})}$ are respectively given by

$$P_{\text{EPR}}^{(\text{mit})} = \frac{P_{\text{EPR}}^{(\text{noisy})}}{f^2} - \frac{1 - f^2}{d_D^2 f^2} \quad (22)$$

and

$$F_{\text{EPR}}^{(\text{mit})} = \left[\frac{1}{F_{\text{EPR}}^{(\text{noisy})}} \left(1 + \frac{1 - f^2}{d_D^2 f^2} \right) - d_A^2 \frac{1 - f^2}{d_D^2 f^2} \right]^{-1}. \quad (23)$$

Here, $f \in [0, 1]$ is a parameter characterizing the depolarizing noise in the application of U or U^* (see Appendix A 1 for details). A value of f closer to 1 indicates more accurate execution of the corresponding circuit. We choose the depolarizing parameter as $f = (1 - p_{2Q}^{(\text{ent})}(\theta))^{N_{2Q}}$, where $p_{2Q}^{(\text{ent})}(\theta) = \frac{5}{4}p_{2Q}(\theta)$ is the entanglement infidelity and N_{2Q} is the number of the two-qubit gates involved in $(U_F)^m$ [85, 86]. This choice of f is based on the observation that the butterfly velocity is nearly equal to the light-cone velocity in our Floquet circuits (as can be confirmed from OTOC results in Appendix B), implying that the effective number of the gates affecting the measurements should be nearly equal to the number of the gates within the light cone. The rotation angle of two-qubit gates in $(U_F)^m$ is $|\theta| = JT$, and the number of the corresponding two-qubit gates in $(U_F)^m$ is $N_{2Q} = \{0, 6, 20, 36, 44, 52, 60, 68, 84, 100\}$ for $m = \{0, 2, 4, 6, 7, 8, 9, 10, 12, 14\}$. This also applies to those in $(U_F^*)^m$. Note that N_{2Q} counts the number of two-qubit gates causally connected to the measurements and thus it is smaller than the total gate count $(N - 1)m = 8m$ in the entire unitary operator for the N -qubit one-dimensional system under open boundary conditions. To highlight the effect of error mitigation, we show P_{EPR} and F_{EPR} subtracted by the exact results, denoted respectively as ΔP_{EPR} and ΔF_{EPR} , in Fig 5.

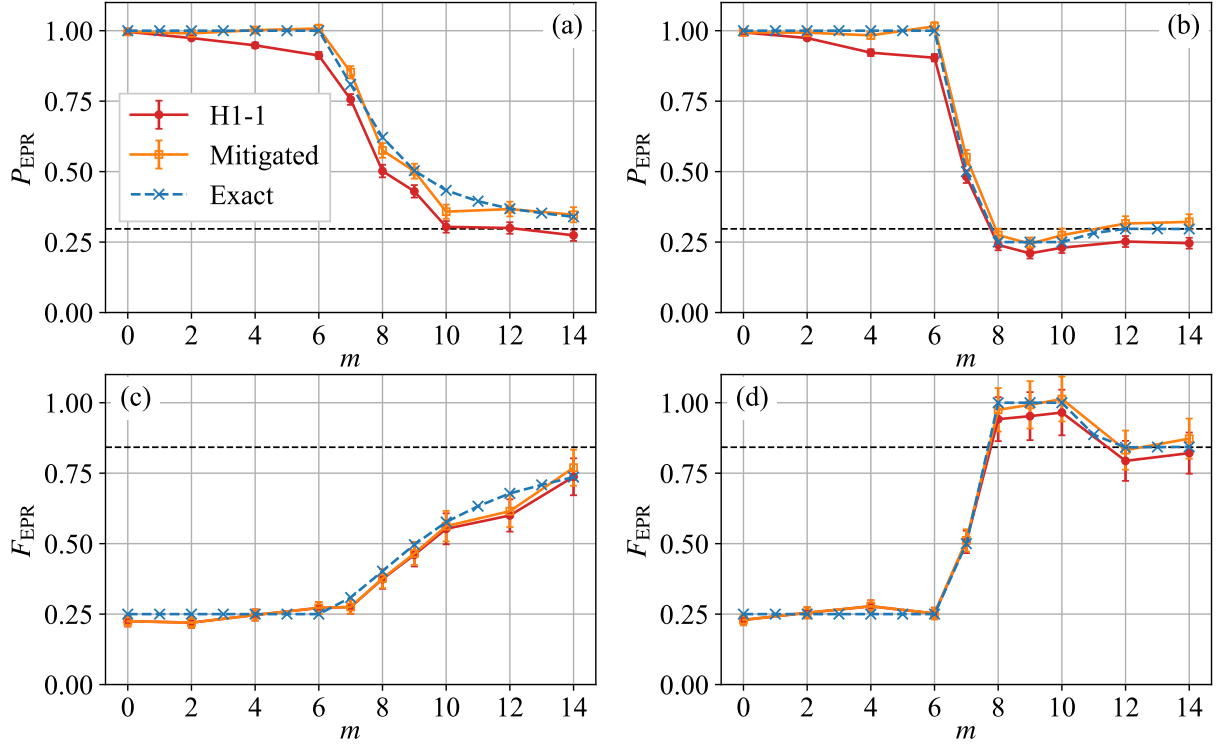


FIG. 4. (a,b) The post-selection probability P_{EPR} and (c,d) the recovery fidelity F_{EPR} of the HPR protocol for the Floquet circuit of (a,c) $JT = 1.3$ and (b,d) $JT = \pi/2$. The red circles show the raw data, $P_{\text{EPR}}^{(\text{noisy})}$ and $F_{\text{EPR}}^{(\text{noisy})}$, of the experiments on the Quantinuum H1-1 system, while the error-mitigated results, $P_{\text{EPR}}^{(\text{mit})}$ and $F_{\text{EPR}}^{(\text{mit})}$, are shown by the orange squares. For comparison, the exact results obtained from classical calculations and also plotted by the blue crosses. The dashed horizontal lines indicate the values obtained with the Haar random unitary circuit used in place of $(U_F)^m$.

In Figs. 4(b) and 4(d), both $P_{\text{EPR}}^{(\text{noisy})}$ and $F_{\text{EPR}}^{(\text{noisy})}$ saturate to values consistent with those from the Haar random unitary, implying the scrambling at late times for $JT = \pi/2$. Conversely, the results for $JT = 1.3$ in Figs. 4(a) and 4(c) do not exhibit saturation to the Haar values up to $m = 14$, indicating slower information scrambling in the Floquet circuit with $JT = 1.3$ compared to $JT = \pi/2$. This observation is consistent with the fact that the parameters at $JT = B_X T = \pi/2$ correspond to a maximally chaotic parametrization [67–70], which we further validate with classical simulations in Appendix B. In the remaining experiments in Sec. IV B and Sec. IV C, we will focus on this maximally chaotic parametrization.

The improved agreements between the experimental results and the exact results upon applying the error mitigation [Fig. 5] imply that the noise effects on P_{EPR} and F_{EPR} are primarily captured by the depolarizing noise channel. The less significant improvement of F_{EPR} by error mitigation [Fig. 5(c,d)] is again consistent with the robustness of F_{EPR} against incoherent noise as compared with P_{EPR} . In Fig. 4, we observe that the mitigation works better for the data with $JT = \pi/2$ than for the data with $JT = 1.3$. This can be attributed to the property of the circuit, where the scrambling unitary operation converts local coherent errors into global incoherent errors [87, 88]. Thus, the global depolarizing

channel would more accurately capture the noise effects of such circuits, which aligns with the fact that the circuit with $JT = \pi/2$ has the particularly strong scrambling property.

B. Out-of-time-ordered correlators

To explore information scrambling in a larger system, we evaluate the evolution of an OTOC with respect to the input state $\rho = |0^N\rangle\langle 0^N|$ and the unitary $U = (U_F)^m$, i.e.,

$$\langle 0^N | (U_F)^{\dagger m} X_n (U_F)^m Z_1 (U_F)^{\dagger m} X_n (U_F)^m Z_1 | 0^N \rangle. \quad (24)$$

It should be noted that, when we construct the corresponding quantum circuit, the right-most Z_1 is omitted based on the fact that $Z_1 |0^N\rangle = |0^N\rangle$. We consider a one-dimensional system consisting of $N = 19$ qubits under open boundary conditions. Adding a single ancillary qubit for the interferometry (see Fig. 3), we make use of all the 20 qubits of the Quantinuum H1-2 system. We run 500 shots of the circuit for each data point with a different time step m . The sizes of measurement and butterfly operators are set to $N_A = 1$ and $N_D = 1$, respectively. The measurement operator O_A is fixed to Z_1 and the site n of the butterfly operator $O_D = X_n$ is varied in the range of $1 \leq n \leq 12$ to explore how the information propagates. Although it is desirable to vary n up to N to fully

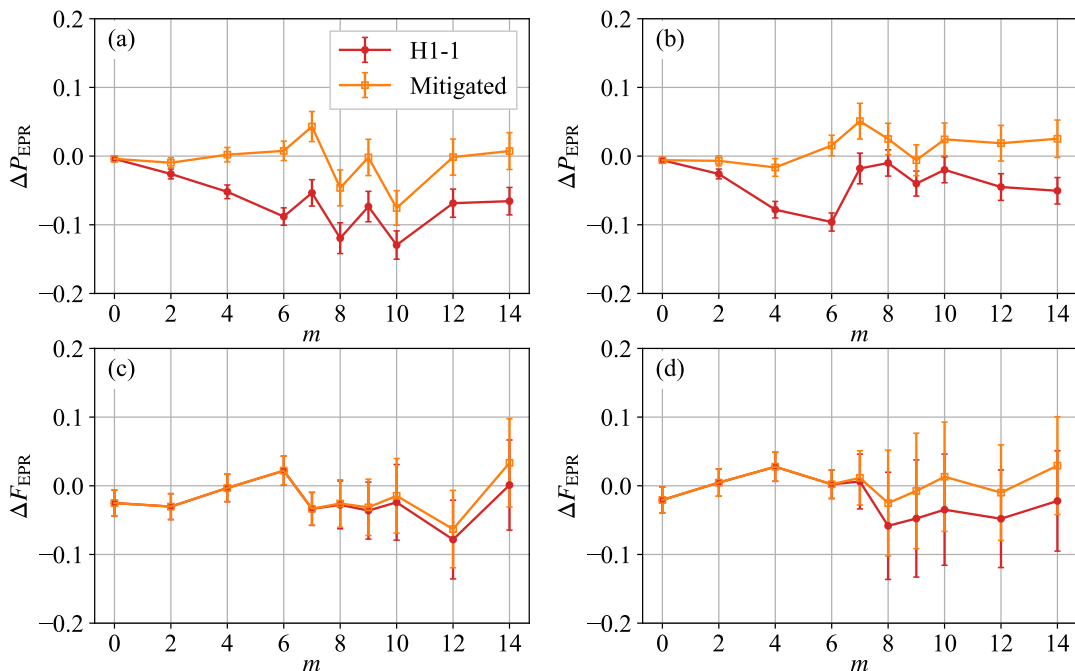


FIG. 5. (a,b) The post-selection probability subtracted by the exact results, ΔP_{EPR} , and (c,d) the recovery fidelity subtracted by the exact results, ΔF_{EPR} , as a function of the Floquet cycles m for (a,c) $JT = 1.3$ and (b,d) $JT = \pi/2$. The red circles and orange squares show the raw and the error-mitigated data, respectively, subtracted by the exact results.

study the information propagation in the entire system, we restrict the range of n as mentioned above due to the limitations of quantum computing resources available to us. We set the driving period $JT = \pi/2$ and the Hamiltonian parameters $(B_X/J, B_Z/J) = (1, 1.3)$. The circuits with $n = 10$ and 11 contain the maximum number of two-qubit gates, 367, inside the causal cone when $m = 15$.

In the raw data shown in Fig. 6(a), a sharp drop of the OTOCs around $m = n$ is observed, followed by remaining around zero. This behaviour is consistent with the ballistic operator growth in a geometrically local circuit and scrambling at late times. To mitigate the noise effect, we additionally compute the normalization factor by running the circuit where the butterfly operator X_n is removed while the rest of the circuit remains the same. The normalization factor becomes 1 in the absence of noise [8, 41] (also see Appendix A 2). Figure 6 (b) shows the normalized OTOCs, the raw data divided by the normalization value. The agreement with the exact results is improved at early times by the mitigation. However, the normalization induces larger variances of the mitigated estimators, which particularly amplifies the statistical fluctuation at late times.

To visualize the ballistic growth of the butterfly operator more effectively, Fig. 7 shows the OTOCs as functions of the position n of the butterfly operator (on the horizontal axis) and the number m of Floquet cycles (on the vertical axis). The results shown in Fig. 7 are identical to those in Fig. 6, but the statistical errors are disregarded to enhance clarity. The causal-cone structure of the one-dimensional system with adjacent interactions, characterized by the abrupt drop of the OTOCs at

$m = n - 1$, is already observed in the raw data [see Fig. 7(a)]. In the normalized OTOCs, the gradual decrease in the absolute value of the OTOC observed in the raw data for $n \geq 8$ and $m \leq n - 1$ is corrected, as shown in Fig. 7(b), resulting in improved agreement with the exact results [see Fig. 7(c)]. The effect of the error mitigation is highlighted in Figs. 7(d,e). We observe that the mitigation improves the agreement with the exact results around the light front for $n \geq 8$. On the other hand, we also observe a slight increase in error away from the light front after applying the mitigation. This is attributed to the increased statistical error due to the mitigation, as discussed for the OTOC results at late times shown in Fig. 6. A systematic analysis of OTOCs for other parameters using classical calculations is provided in Appendix B.

C. Application: thermal expectation value

As an application of the Floquet scrambling circuit, we evaluate the expectation value of $O = Z_1 Z_2$ within the microcanonical ensemble of the one-dimensional spin-1/2 isotropic Heisenberg model, employing the protocol described in Sec. III C. The Hamiltonian is given by

$$\mathcal{H}_{\text{XXX}} = \frac{\mathcal{J}}{2} \sum_{i=1}^N (X_i X_{i+1} + Y_i Y_{i+1} + Z_i Z_{i+1} + I_i I_{i+1}) \quad (25)$$

under periodic boundary conditions, where the $N + 1$ th and 1st sites are identified. We evaluate the Loschmidt amplitude

$$\mathcal{L}(s\Delta t) = \langle \psi(m) | e^{-i\mathcal{H}_{\text{even}} s\Delta t} e^{-i\mathcal{H}_{\text{odd}} s\Delta t} | \psi(m) \rangle \quad (26)$$

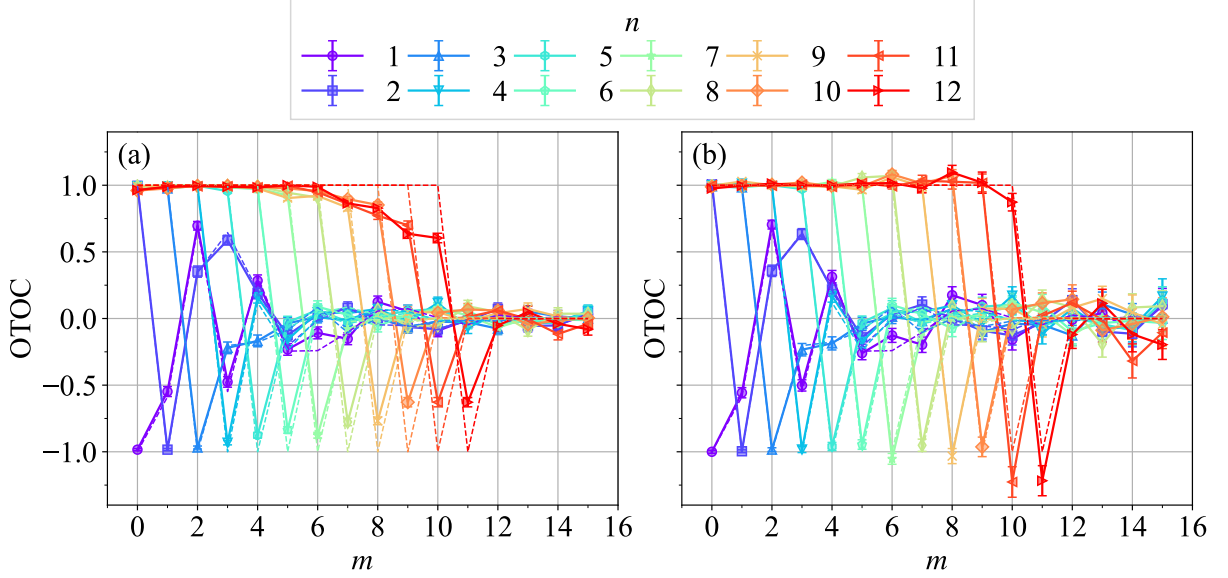


FIG. 6. OTOCs defined in Eq. (24) plotted as a function of the number m of Floquet cycles (horizontal axis) for various positions n of the butterfly operator. (a) The raw data obtained through experiments performed on the Quantinuum H1-2 system and (b) the error-mitigated results. Dashed lines represent the exact results obtained from classical calculations. The one-dimensional chain consisting of $N = 19$ spins under open boundary conditions is considered.

and the corresponding amplitude

$$\mathcal{L}_{Z_1 Z_2}(s\Delta t) = \langle \psi(m) | Z_1 Z_2 e^{-i\mathcal{H}_{\text{even}} s\Delta t} e^{-i\mathcal{H}_{\text{odd}} s\Delta t} | \psi(m) \rangle \quad (27)$$

using the state evolved with the Floquet circuit, where $|\psi(m)\rangle = (U_F)^m |\psi_0\rangle$ and $\mathcal{H}_{\text{even/odd}} = (\mathcal{J}/2) \sum_{i:\text{even/odd}} (X_i X_{i+1} + Y_i Y_{i+1} + Z_i Z_{i+1} + I_i I_{i+1})$. The initial product state $|\psi_0\rangle$ is prepared as $|\psi_0\rangle = \prod_{i=1}^N e^{-i\phi_i Y_i/2} |0^N\rangle$, where $\{\phi_i\}_{i=1}^N$ is a set of independent random angles, each of which is drawn uniformly from $[0, 4\pi)$. We consider a system of $N = 16$ qubits and set the number of Floquet cycles to $m = 8$ and $m = 16$ so that $|\psi(m)\rangle$ approximately forms a state 2-design under periodic boundary conditions (see Appendix C).

As already indicated in Eqs. (26) and (27), to evaluate the two amplitudes $\mathcal{L}(t)$ and $\mathcal{L}_{Z_1 Z_2}(t)$ with $t = s\Delta t$, we approximate the time-evolution operator $e^{-i\mathcal{H}_{\text{xxx}} s\Delta t}$ by a single-step first-order product (Trotter) formula, $e^{-i\mathcal{H}_{\text{xxx}} s\Delta t} \simeq e^{-i\mathcal{H}_{\text{even}} s\Delta t} e^{-i\mathcal{H}_{\text{odd}} s\Delta t}$. The computed amplitudes are then classically post-processed as in Eqs. (18) and (19) with $S = 40$ and $\Delta t = 0.05/\mathcal{J}$. The real and imaginary parts of $\mathcal{L}(t)$ and $\mathcal{L}_{Z_1 Z_2}(t)$ are estimated separately with the Hadamard-test circuits (see Fig. 8) on the Quantinuum H1-2 system. For the trace estimation, we generate eight instances of the Floquet scrambled states $|\psi(m)\rangle$, consisting of four independent realizations of $|\psi_0\rangle$ and two Floquet cycles $m = 8$ and $m = 16$. We take 100 shots to evaluate $\mathcal{L}(t)$ and $\mathcal{L}_{Z_1 Z_2}(t)$ for each instance of $|\psi(m)\rangle$, thus taking 800 shots in total at each data point. Furthermore, we symmetrize (antisymmetrize) the real (imaginary) parts of $\mathcal{L}(t)$ and $\mathcal{L}_{Z_1 Z_2}(t)$ with respect to t by using the data obtained for $t > 0$ and $t < 0$. The symmetrizations (antisymmetrizations) are made so that $\mathcal{L}(t)$ and $\mathcal{L}_{Z_1 Z_2}(t)$ share with $\text{Tr}[e^{-i\mathcal{H}_{\text{xxx}} t}]/d$ and $\text{Tr}[Z_1 Z_2 e^{-i\mathcal{H}_{\text{xxx}} t}]/d$ the common property that their real (imaginary) parts are even (odd) functions

of t . Here, $d = 2^N$ is the dimension of the Hilbert space for the system \mathcal{H}_{xxx} . For this reason, we will only show the results for $t \geq 0$.

We note a previous study [89] using a similar Hadamard-test circuit on entangled random states to assess the density of states in spin chains comprising 12 and 18 spins, performed using the Quantinuum H1-1 system. Additionally, a more recent study evaluated the Loschmidt amplitude of the Fermi-Hubbard model with 32 orbitals in reference to product states using the Quantinuum H2-1 system, as reported in Ref. [90]. They estimated the microcanonical expectation value of the double occupancy using the importance sampling techniques on initial product states [73–76]. Here, we further proceed in this direction by evaluating the microcanonical expectation value of the spin correlation function $\langle Z_1 Z_2 \rangle^{(\text{est})}$ for the Heisenberg spin chain.

Figures 9(a) and 9(b) show the Loschmidt amplitude $\mathcal{L}(t)$ obtained from the experiments using the Quantinuum H1-2 system and the associated density of states $D(E)$ evaluated via Eq. (19), respectively. For comparison, we carry out classical calculations of the Loschmidt amplitude, labeled as “Exact” in the figures, where $|\psi(m)\rangle$ is substituted by a Haar-random state and the results are averaged over eight instances of Haar-random states. Qualitative agreement with the classical results is observed without error mitigation. The parameter σ in Eq. (19) [also see Eq. (10)] is selected as

$$\sigma = \frac{\sigma_{\mathcal{H}}}{\sqrt{2\pi}}, \quad (28)$$

where

$$\sigma_{\mathcal{H}}^2 := \frac{1}{d} \text{Tr}[\mathcal{H}_{\text{xxx}}^2] - \left(\frac{1}{d} \text{Tr}[\mathcal{H}_{\text{xxx}}] \right)^2 \quad (29)$$

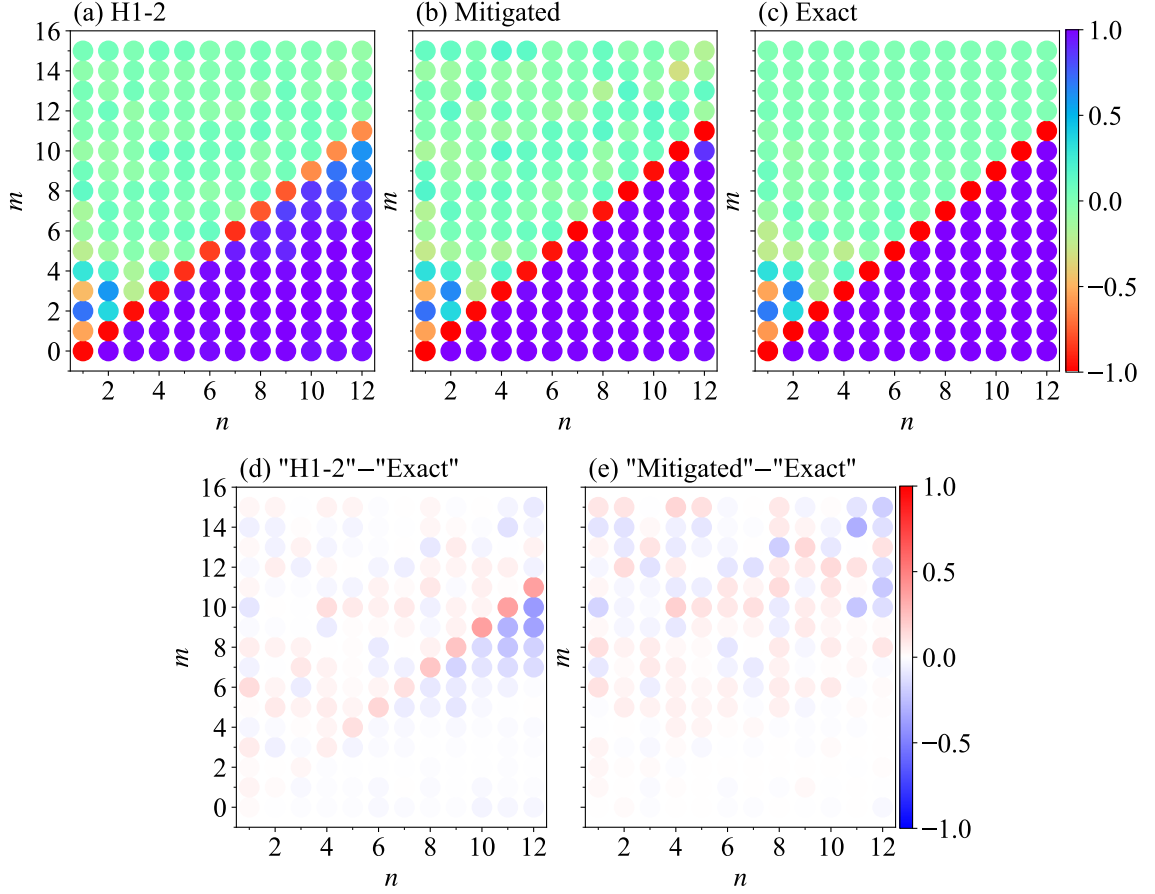


FIG. 7. OTOCs defined in Eq. (24) plotted as functions of the position n of the butterfly operator (horizontal axis) and the number m of Floquet cycles (vertical axis). (a) The raw data obtained through experiments performed on the Quantinuum H1-2 system, (b) the error-mitigated data, and (c) the exact results obtained from classical calculations. The data presented here are the same as those in Fig. 6. The raw and the mitigated data subtracted by the exact data are shown in (d) and (e), respectively.

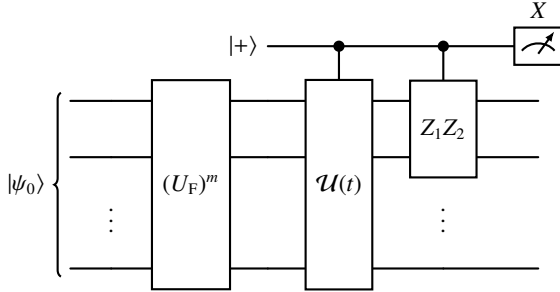


FIG. 8. The quantum circuit used to calculate the real part of $\mathcal{L}_{Z_1 Z_2}(s\Delta t)$ in Eq. (27), where $\mathcal{U}(t) := e^{-i\mathcal{H}_{\text{even}}s\Delta t} e^{-i\mathcal{H}_{\text{odd}}s\Delta t}$. The top qubit is the single-qubit ancillary register initialized to $|+\rangle$, while the remaining qubits constitute the system register with the input state $|\psi_0\rangle$. At the end of the circuit, the ancillary qubit is measured in the X basis. The imaginary part is calculated by employing the same circuit with the measurement basis X replaced by the Y basis.

is the energy variance with respect to the maximally mixed state, and the factor $1/\sqrt{2\pi}$ is introduced accordingly to the definition of the width of the energy window described in

Ref. [55]. The selection of σ is motivated by the notion that $\sigma_{\mathcal{H}}$ roughly signifies the breadth of the density of states in energy, suggesting that the Loschmidt amplitude decays around the time $t \sim \sigma_{\mathcal{H}}^{-1}$ (for details, see Appendix C). Moreover, the variance $\sigma_{\mathcal{H}}^2$ scales linearly with the system size N , ensuring the convergence of $\langle O \rangle$ in Eq. (10) towards the correct value in the thermodynamic limit. In the present case with $N = 16$, the energy variance is determined as $\sigma_{\mathcal{H}}^2 = 12\mathcal{J}^2$, resulting in $\sigma = \sqrt{6/\pi}\mathcal{J} \approx 1.38\mathcal{J}$.

Figure 9(c) shows the microcanonical expectation value of the spin correlation function $\langle Z_1 Z_2 \rangle^{(\text{est})}$ [also see Eqs. (12) and (20)]. Here, we have evaluated $\mathcal{L}_{Z_1 Z_2}(t)$ and $D_{Z_1 Z_2}(E)$ in a manner similar to $\mathcal{L}(t)$ and $D(E)$. The experimental results of $\mathcal{L}_{Z_1 Z_2}(t)$ using the Quantinuum H1-2 system and the associated $D_{Z_1 Z_2}(E)$ are provided in Appendix F. We observe a good agreement with the exact results within the statistical uncertainty for the energy range $E_{\infty} - \sigma_{\mathcal{H}} \lesssim E \lesssim E_{\infty} + \sigma_{\mathcal{H}}$, which lies between the two vertical dashed lines in Figs. 9(b) and 9(c). Here, $E_{\infty} := \text{Tr}[\mathcal{H}_{XXX}]/d = N\mathcal{J}/2$ is the energy corresponding to the maximally mixed state, or equivalently the energy at infinite temperature, at which $\langle Z_1 Z_2 \rangle^{(\text{est})}$

changes its sign. This sign change can be understood by noting that the correlation vanishes at infinite temperature. Furthermore, the nearest-neighbor spin correlation is antiferromagnetic at positive temperatures, resulting in $\langle Z_1 Z_2 \rangle^{(\text{est})} < 0$ for $E \lesssim E_\infty$, and ferromagnetic at negative temperatures, resulting in $\langle Z_1 Z_2 \rangle^{(\text{est})} > 0$ for $E \gtrsim E_\infty$.⁴ The sign structure of $\langle Z_1 Z_2 \rangle^{(\text{est})}$ around E_∞ is thus correctly captured by the experimental results.

The agreement for $E_\infty - \sigma_{\mathcal{H}} \lesssim E \lesssim E_\infty + \sigma_{\mathcal{H}}$ is attributed to the concentration of the density of states in this energy span, as shown in Fig. 9(b), where $D(E)$ peaks around E_∞ with a width $\sigma_{\mathcal{H}}$. Indeed, the density of states $D(E)$ decays rapidly beyond this energy range. The decay of $D(E)$ implies an increase in the purity $\text{Tr}[\rho_\sigma(E)^2]$ of the associated microcanonical density matrix. This, in turn, leads to an increase in the failure probability in Eq. (13) (also see Appendix D) as well as the shot noise in $\langle Z_1 Z_2 \rangle^{(\text{est})}$ (for details, see Appendix E). This explains the deviation from the exact results with larger statistical errors beyond this energy range. Finally, we observe that the density of states shown in Fig. 9(b) are less accurate than the thermal expectation values in Fig. 9(c) within the range $E_\infty - \sigma_{\mathcal{H}} \lesssim E \lesssim E_\infty + \sigma_{\mathcal{H}}$. The better results in Fig. 9(c) are attributed to the cancellation of depolarizing noise effects between the numerator $D_{Z_1 Z_2}(E)$ and denominator $D(E)$ in the thermal expectation value $\langle Z_1 Z_2 \rangle^{(\text{est})} = D_{Z_1 Z_2}(E)/D(E)$.

V. DISCUSSION

We performed three experiments on trapped-ion quantum computers: the HPR protocol, the interferometric protocol, and the calculation of the thermal expectation value of a local operator. In the first two experiments, we characterized the information scrambling of the kicked-Ising model at and around the self-dual point. The HPR protocol involved manipulating two copies of the 9-qubit spin chains augmented by a two-qubit ancillary register, resulting in a total of 20 qubits. We verified the high-fidelity teleportation of quantum information, as expected from the chaotic unitary dynamics. Additionally, We tested the incoherent error mitigation assuming the depolarizing noise model. The improved performance with the mitigation suggests that the depolarizing noise model effectively captures the influence of the noise on the HPR protocol.

In the second experiment, we scaled up the system size to 19 qubits and calculated the OTOCs using the interferometric protocol. Successful execution of the circuits confirmed the sharp decay of OTOCs at late times, consistent with theoretical predictions. Despite the maximum two-qubit gate count being as large as 367 inside the causal cone of the measured qubits, we observed agreements between the experimental data and the exact numerical values. Lastly, having confirmed the scrambling property of the unitary circuits, we employed

them to calculate the thermal expectation values of local operators, borrowing the idea of microcanonical TPQ states.

While the present studies nicely demonstrate the capability of currently available quantum devices and the proposed quantum algorithms, there is still the question of how far these protocols can be scaled up to potentially reach the realm of classically intractable system sizes and evolution times. Foreseeing the interferometric experiments on larger systems, let us make a rough estimate of the required resources. Recall that our 20-qubit interferometric circuit for the kicked Ising model under open boundary conditions contains at most 367 two-qubit gates inside the causal cone. Assuming the dominant source of error is two-qubit gate operations, with their average gate infidelity of 0.1%, we now discuss the fidelity of a 60-qubit interferometric circuit. For the same one-dimensional geometrically local model under periodic boundary conditions to exhibit scrambling, the Floquet system needs to evolve for $3/2$ times more cycles than the 20-qubit system with open boundary conditions. This leads to a two-qubit gate counts of $367 \times 3 \times 3/2 \approx 1652$. Consequently, the circuit fidelity is roughly estimated as $f \sim 0.999^{1652} \approx 0.2$. Evaluating the normalized OTOC with a statistical uncertainty ϵ requires a shot overhead of $O((f\epsilon)^{-2})$. Alternatively, one can introduce long-range interactions to reduce the scrambling time, which is suitable for the hardware equipped with long-range connectivity. For instance, fast scrambling systems like the Sachdev–Ye–Kitaev model [91–93] have a scrambling time $O(\log N)$, contrasting with N in geometrically local systems. We leave more comprehensive studies for larger-scale experiments in the future.

DATA AVAILABILITY

The data that support the findings of this study are available at Zenodo [94].

CODE AVAILABILITY

The code used to create the figures in this paper is available from the authors upon reasonable request.

ACKNOWLEDGMENTS

Y.K. is grateful to Luuk Coopmans, Matthew DeCross, Henrik Dreyer, Michael Foss-Feig, Etienne Granet, Enrico Rinaldi, Matthias Rosenkranz, Kentaro Yamamoto, and Yasuyoshi Yonezawa for fruitful discussions. A portion of this work is based on results obtained from project JPNP20017, subsidized by the New Energy and Industrial Technology Development Organization (NEDO). This study is also supported by JSPS KAKENHI Grants No. JP19K23433, No. JP21H01007, No. JP21H01084, No. JP21H04446, No. JP22K03520, and No. JP24K00630. We are also grateful for the funding received from JST COI-NEXT (Grant No. JPMJPF2221) and the Program for Promoting Research of

⁴ In general, negative-temperature states, corresponding to $E \geq E_\infty$, are not realized in thermal equilibrium but can be realized as nonequilibrium states.

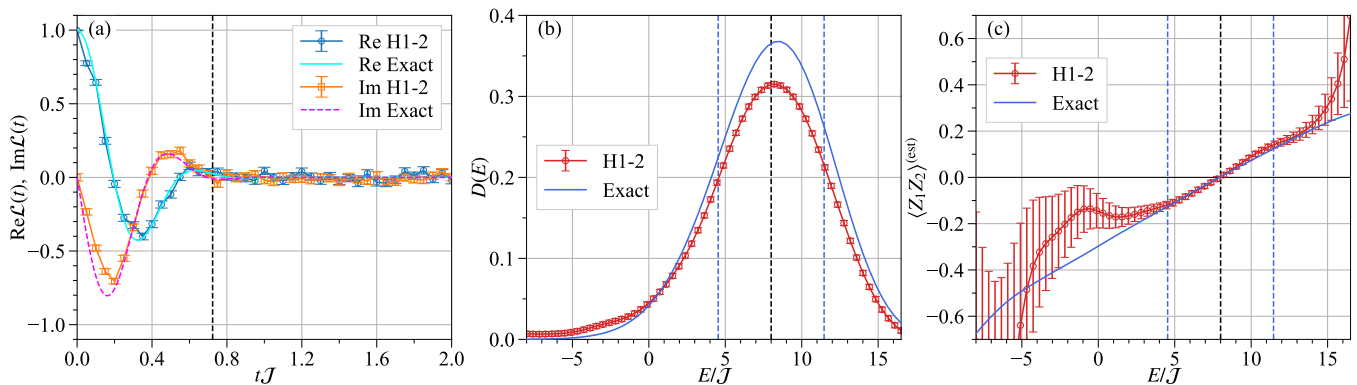


FIG. 9. (a) Real and imaginary parts of the Loschmidt amplitude $\mathcal{L}(t)$ for the one-dimensional Heisenberg model \mathcal{H}_{XXX} with $N = 16$ sites under periodic boundary conditions. These experimental results are obtained for the Floquet scrambled states $|\psi(m)\rangle$ with $m = 8$ and 16 using the Quantum H1-2 system. The vertical line indicates $t = \sigma^{-1}$, where σ is defined in Eq. (28). For comparison, the ideal values obtained from classical calculations are also shown by solid and dashed curves, for the real and imaginary parts, respectively. (b) Density of states $D(E)$ obtained via Eq. (19) as a Fourier transform of the Gaussian-weighted Loschmidt amplitude $\mathcal{L}(t)$ shown in (a). (c) Microcanonical expectation value of the nearest-neighbor spin correlation function $\langle Z_1 Z_2 \rangle^{(\text{est})}$ for the one-dimensional Heisenberg model \mathcal{H}_{XXX} with $N = 16$ sites under periodic boundary conditions (also see Appendix F). In (b) and (c), the black dashed vertical line indicates $E = E_\infty = 8J$, and the blue dashed vertical lines indicate $E = E_\infty \pm \sigma_H = 8J \pm 2\sqrt{3}J$, where σ_H is defined in Eq. (29). In (b) and (c), the ideal values obtained from classical calculations are also shown by blue solid curves.

the Supercomputer Fugaku (Grant No. MXP1020230411) from MEXT, Japan. Additionally, we acknowledge the support from the UTokyo Quantum Initiative, the RIKEN TRIP project, and the COE research grant in computational science from Hyogo Prefecture and Kobe City through the Foundation for Computational Science. A part of the numerical simulations has been performed using the HOKUSAI supercomputer at RIKEN, cluster computers at iTHEMS in RIKEN, and Yukawa-21 at YITP in Kyoto University.

AUTHOR CONTRIBUTIONS

K.S., Y.K., and T.H. conceived and designed the study. K.S., Y.K., and T.H. performed analytic calculations, and K.S.

carried out numerical studies and hardware experiments. All authors analysed the data, created the figures, interpreted the results and wrote the manuscript.

COMPETING INTERESTS

The authors declare no competing financial or non-financial interests.

-
- [1] P. Hayden and J. Preskill, Black holes as mirrors: Quantum information in random subsystems, *Journal of High Energy Physics* **2007**, 120 (2007).
 - [2] Y. Sekino and L. Susskind, Fast scramblers, *Journal of High Energy Physics* **2008**, 065 (2008).
 - [3] S. H. Shenker and D. Stanford, Black holes and the butterfly effect, *Journal of High Energy Physics* **2014**, 067 (2014).
 - [4] S. H. Shenker and D. Stanford, Stringy effects in scrambling, *Journal of High Energy Physics* **2015**, 132 (2015).
 - [5] J. Maldacena, S. H. Shenker, and D. Stanford, A bound on chaos, *Journal of High Energy Physics* **2016**, 106 (2016).
 - [6] P. Hosur, X.-L. Qi, D. A. Roberts, and B. Yoshida, Chaos in quantum channels, *Journal of High Energy Physics* **2016**, 004 (2016).
 - [7] D. A. Roberts and B. Yoshida, Chaos and complexity by design, *Journal of High Energy Physics* **2017**, 121 (2017).
 - [8] B. Swingle and N. Yunger Halpern, Resilience of scrambling measurements, *Phys. Rev. A* **97**, 062113 (2018).
 - [9] S. Xu and B. Swingle, Scrambling Dynamics and Out-of-Time-Ordered Correlators in Quantum Many-Body Systems, *PRX Quantum* **5**, 010201 (2024).
 - [10] M. V. Berry, Semiclassical theory of spectral rigidity, *Proceedings of the Royal Society of London. A. Mathematical and Physical Sciences* **400**, 229 (1985).
 - [11] M. Sieber and K. Richter, Correlations between periodic orbits and their rôle in spectral statistics, *Physica Scripta* **2001**, 128 (2001).
 - [12] M. Sieber, Leading off-diagonal approximation for the spectral form factor for uniformly hyperbolic systems, *Journal of Physics A: Mathematical and General* **35**, L613 (2002).
 - [13] S. Müller, S. Heusler, P. Braun, F. Haake, and A. Altland, Semiclassical Foundation of Universality in Quantum Chaos,

- Phys. Rev. Lett.* **93**, 014103 (2004).
- [14] A. Peres, Stability of quantum motion in chaotic and regular systems, *Phys. Rev. A* **30**, 1610 (1984).
- [15] A. Goussev, R. A. Jalabert, H. M. Pastawski, and D. Wisniacki, Loschmidt echo (2012), [arXiv:1206.6348](https://arxiv.org/abs/1206.6348).
- [16] T. Gorin, T. c. v. Prosen, T. H. Seligman, and M. Žnidarič, Dynamics of loschmidt echoes and fidelity decay, *Physics Reports* **435**, 33 (2006).
- [17] A. I. Larkin and Y. N. Ovchinnikov, Quasiclassical Method in the Theory of Superconductivity, *Soviet Journal of Experimental and Theoretical Physics* **28**, 1200 (1969).
- [18] D. A. Roberts, D. Stanford, and L. Susskind, Localized shocks, *Journal of High Energy Physics* **2015**, 051 (2015).
- [19] B. Swingle, Unscrambling the physics of out-of-time-order correlators, *Nature Phys.* **14**, 988 (2018).
- [20] T. c. v. Prosen, General relation between quantum ergodicity and fidelity of quantum dynamics, *Phys. Rev. E* **65**, 036208 (2002).
- [21] T. c. v. Prosen, Chaos and complexity of quantum motion, *Journal of Physics A: Mathematical and Theoretical* **40**, 7881 (2007).
- [22] A. Lazarides, A. Das, and R. Moessner, Equilibrium states of generic quantum systems subject to periodic driving, *Phys. Rev. E* **90**, 012110 (2014).
- [23] L. D'Alessio and M. Rigol, Long-time behavior of isolated periodically driven interacting lattice systems, *Phys. Rev. X* **4**, 041048 (2014).
- [24] D. A. Abanin, W. De Roeck, and F. m. c. Huvneers, Exponentially slow heating in periodically driven many-body systems, *Phys. Rev. Lett.* **115**, 256803 (2015).
- [25] T. Mori, T. Kuwahara, and K. Saito, Rigorous bound on energy absorption and generic relaxation in periodically driven quantum systems, *Phys. Rev. Lett.* **116**, 120401 (2016).
- [26] T. Kuwahara, T. Mori, and K. Saito, Floquet–magnus theory and generic transient dynamics in periodically driven many-body quantum systems, *Annals of Physics* **367**, 96 (2016).
- [27] T. Mori, T. N. Ikeda, E. Kaminishi, and M. Ueda, Thermalization and prethermalization in isolated quantum systems: a theoretical overview, *Journal of Physics B: Atomic, Molecular and Optical Physics* **51**, 112001 (2018).
- [28] T. Eckstein, R. Mansuroglu, P. Czarnik, J.-X. Zhu, M. J. Hartmann, L. Cincio, A. T. Sornborger, and Z. Holmes, Large-scale simulations of Floquet physics on near-term quantum computers (2023), [arXiv:2303.02209](https://arxiv.org/abs/2303.02209) [quant-ph].
- [29] B. Yoshida and A. Kitaev, Efficient decoding for the Hayden-Preskill protocol (2017), [arXiv:1710.03363](https://arxiv.org/abs/1710.03363) [hep-th].
- [30] B. Yoshida and N. Y. Yao, Disentangling scrambling and decoherence via quantum teleportation, *Phys. Rev. X* **9**, 011006 (2019).
- [31] K. A. Landsman, C. Figgatt, T. Schuster, N. M. Linke, B. Yoshida, N. Y. Yao, and C. Monroe, Verified Quantum Information Scrambling, *Nature* **567**, 61 (2019).
- [32] M. S. Blok, V. V. Ramasesh, T. Schuster, K. O'Brien, J. M. Kreikebaum, D. Dahlen, A. Morvan, B. Yoshida, N. Y. Yao, and I. Siddiqi, Quantum information scrambling on a superconducting qutrit processor, *Phys. Rev. X* **11**, 021010 (2021).
- [33] I. Shapoval, V. P. Su, W. de Jong, M. Urbanek, and B. Swingle, Towards Quantum Gravity in the Lab on Quantum Processors, *Quantum* **7**, 1138 (2023).
- [34] D. Jafferis, A. Zlokapa, J. D. Lykken, D. K. Kolchmeyer, S. I. Davis, N. Lauk, H. Neven, and M. Spiropulu, Traversable wormhole dynamics on a quantum processor, *Nature* **612**, 51 (2022).
- [35] N. Bao and Y. Kikuchi, Hayden-Preskill decoding from noisy Hawking radiation, *Journal of High Energy Physics* **2021**, 017 (2021).
- [36] T. Hayata, Y. Hidaka, and Y. Kikuchi, Diagnosis of information scrambling from hamiltonian evolution under decoherence, *Phys. Rev. D* **104**, 074518 (2021).
- [37] B. Swingle, G. Bentsen, M. Schleier-Smith, and P. Hayden, Measuring the scrambling of quantum information, *Phys. Rev. A* **94**, 040302 (2016).
- [38] J. Li, R. Fan, H. Wang, B. Ye, B. Zeng, H. Zhai, X. Peng, and J. Du, Measuring out-of-time-order correlators on a nuclear magnetic resonance quantum simulator, *Phys. Rev. X* **7**, 031011 (2017).
- [39] M. Gärttner, J. G. Bohnet, A. Safavi-Naini, M. L. Wall, J. J. Bollinger, and A. M. Rey, Measuring out-of-time-order correlations and multiple quantum spectra in a trapped ion quantum magnet, *Nature Phys.* **13**, 781 (2017).
- [40] M. K. Joshi, A. Elben, B. Vermersch, T. Brydges, C. Maier, P. Zoller, R. Blatt, and C. F. Roos, Quantum information scrambling in a trapped-ion quantum simulator with tunable range interactions, *Phys. Rev. Lett.* **124**, 240505 (2020).
- [41] X. Mi, P. Roushan, C. Quintana, S. Mandrà, J. Marshall, C. Neill, F. Arute, K. Arya, J. Atalaya, R. Babbush, J. C. Bardin, R. Barends, J. Basso, A. Bengtsson, S. Boixo, A. Bourassa, M. Broughton, B. B. Buckley, D. A. Buell, B. Burkett, N. Bushnell, Z. Chen, B. Chiaro, R. Collins, W. Courtney, S. Demura, A. R. Derk, A. Dunsworth, D. Eppens, C. Erickson, E. Farhi, A. G. Fowler, B. Foxen, C. Gidney, M. Giustina, J. A. Gross, M. P. Harrigan, S. D. Harrington, J. Hilton, A. Ho, S. Hong, T. Huang, W. J. Huggins, L. B. Ioffe, S. V. Isakov, E. Jeffrey, Z. Jiang, C. Jones, D. Kafri, J. Kelly, S. Kim, A. Kitaev, P. V. Klimov, A. N. Korotkov, F. Kostritsa, D. Landhuis, P. Laptev, E. Lucero, O. Martin, J. R. McClean, T. McCourt, M. McEwen, A. Megrant, K. C. Miao, M. Mohseni, S. Montazeri, W. Mruczkiewicz, J. Mutus, O. Naaman, M. Neeley, M. Newman, M. Y. Niu, T. E. O'Brien, A. Opremcak, E. Ostby, B. Pato, A. Petukhov, N. Redd, N. C. Rubin, D. Sank, K. J. Satzinger, V. Shvarts, D. Strain, M. Szalay, M. D. Trevithick, B. Villalonga, T. White, Z. J. Yao, P. Yeh, A. Zalcman, H. Neven, I. Aleiner, K. Kechedzhi, V. Smelyanskiy, and Y. Chen, Information scrambling in quantum circuits, *Science* **374**, 1479 (2021).
- [42] M. Asaduzzaman, R. G. Jha, and B. Sambasivam, A model of quantum gravity on a noisy quantum computer (2023), [arXiv:2311.17991](https://arxiv.org/abs/2311.17991) [quant-ph].
- [43] P. Bocchieri and A. Loinger, Ergodic foundation of quantum statistical mechanics, *Phys. Rev.* **114**, 948 (1959).
- [44] J. Jaklič and P. Prelošek, Lanczos method for the calculation of finite-temperature quantities in correlated systems, *Phys. Rev. B* **49**, 5065 (1994).
- [45] J. Jaklič and P. Prelovšek, Finite-temperature properties of doped antiferromagnets, *Adv. Phys.* **49**, 1 (2000).
- [46] A. Hams and H. De Raedt, Fast algorithm for finding the eigenvalue distribution of very large matrices, *Phys. Rev. E* **62**, 4365 (2000).
- [47] T. Iitaka and T. Ebisuzaki, Random phase vector for calculating the trace of a large matrix, *Phys. Rev. E* **69**, 057701 (2004).
- [48] S. Popescu, A. J. Short, and A. Winter, Entanglement and the foundations of statistical mechanics, *Nature Physics* **2**, 1745 (2000).
- [49] S. Sugiura and A. Shimizu, Thermal Pure Quantum States at Finite Temperature, *Phys. Rev. Lett.* **108**, 240401 (2012).
- [50] S. Sugiura and A. Shimizu, Canonical Thermal Pure Quantum State, *Phys. Rev. Lett.* **111**, 010401 (2013).

- [51] S. Sugiura, *Formulation of Statistical Mechanics Based on Thermal Pure Quantum States*, Springer Theses (Springer Nature Singapore, 2017).
- [52] Y. Nakata, C. Hirche, C. Morgan, and A. Winter, Unitary 2-designs from random X - and Z -diagonal unitaries, *Journal of Mathematical Physics* **58**, 052203 (2017).
- [53] F. Jin, D. Willsch, M. Willsch, H. Lagemann, K. Michielsen, and H. De Raedt, Random State Technology, *Journal of the Physical Society of Japan* **90**, 012001 (2021).
- [54] J. Richter and A. Pal, Simulating hydrodynamics on noisy intermediate-scale quantum devices with random circuits, *Phys. Rev. Lett.* **126**, 230501 (2021).
- [55] K. Seki and S. Yunoki, Energy-filtered random-phase states as microcanonical thermal pure quantum states, *Phys. Rev. B* **106**, 155111 (2022).
- [56] C. Powers, L. Bassman Otfelie, D. Camps, and W. A. de Jong, Exploring finite temperature properties of materials with quantum computers, *Sci. Rep.* **13**, 1986 (2023).
- [57] L. Coopmans, Y. Kikuchi, and M. Benedetti, Predicting gibbs-state expectation values with pure thermal shadows, *PRX Quantum* **4**, 010305 (2023).
- [58] K. Kaneko, E. Iyoda, and T. Sagawa, Characterizing complexity of many-body quantum dynamics by higher-order eigenstate thermalization, *Phys. Rev. A* **101**, 042126 (2020).
- [59] J. Choi, A. L. Shaw, I. S. Madjarov, X. Xie, R. Finkelstein, J. P. Covey, J. S. Cotler, D. K. Mark, H.-Y. Huang, A. Kale, H. Pichler, F. G. S. L. Brandão, S. Choi, and M. Endres, Preparing random states and benchmarking with many-body quantum chaos, *Nature* **613**, 468 (2023).
- [60] J. S. Cotler, D. K. Mark, H.-Y. Huang, F. Hernández, J. Choi, A. L. Shaw, M. Endres, and S. Choi, Emergent quantum state designs from individual many-body wave functions, *PRX Quantum* **4**, 010311 (2023).
- [61] M. Fava, J. Kurchan, and S. Pappalardi, Designs via Free Probability (2023), [arXiv:2308.06200](https://arxiv.org/abs/2308.06200) [quant-ph].
- [62] S. Lloyd, Universal quantum simulators, *Science* **273**, 1073 (1996), <https://www.science.org/doi/pdf/10.1126/science.273.5278.1073>.
- [63] M. Heyl, P. Hauke, and P. Zoller, Quantum localization bounds trotter errors in digital quantum simulation, *Science Advances* **5**, eaau8342 (2019).
- [64] L. M. Sieberer, T. Olsacher, A. Elben, M. Heyl, P. Hauke, F. Haake, and P. Zoller, Digital quantum simulation, Trotter errors, and quantum chaos of the kicked top, *npj Quantum Information* **5**, 78 (2019).
- [65] E. Vernier, B. Bertini, G. Giudici, and L. Piroli, Integrable digital quantum simulation: Generalized gibbs ensembles and trotter transitions, *Phys. Rev. Lett.* **130**, 260401 (2023).
- [66] K. Shinjo, K. Seki, T. Shirakawa, R.-Y. Sun, and S. Yunoki, Unveiling clean two-dimensional discrete time quasicrystals on a digital quantum computer (2024), [arXiv:2403.16718](https://arxiv.org/abs/2403.16718) [quant-ph].
- [67] B. Bertini, P. Kos, and T. c. v. Prosen, Exact spectral form factor in a minimal model of many-body quantum chaos, *Phys. Rev. Lett.* **121**, 264101 (2018).
- [68] B. Bertini, P. Kos, and T. c. v. Prosen, Operator Entanglement in Local Quantum Circuits I: Chaotic Dual-Unitary Circuits, *SciPost Phys.* **8**, 067 (2020).
- [69] B. Bertini, P. Kos, and T. c. v. Prosen, Entanglement spreading in a minimal model of maximal many-body quantum chaos, *Phys. Rev. X* **9**, 021033 (2019).
- [70] L. Piroli, B. Bertini, J. I. Cirac, and T. c. v. Prosen, Exact dynamics in dual-unitary quantum circuits, *Phys. Rev. B* **101**, 094304 (2020).
- [71] F. G. S. L. Brandão, D. Neuhauser, Extraction, through filter-diagonalization, of general quantum eigenvalues or classical normal mode frequencies from a small number of residues or a short-time segment of a signal. I. Theory and application to a quantum-dynamics model, *The Journal of Chemical Physics* **102**, 8011 (1995).
- [72] A. N. Chowdhury and R. D. Somma, Quantum algorithms for Gibbs sampling and hitting-time estimation, *Quant. Inf. Comput.* **17**, 0041 (2017).
- [73] S. Lu, M. C. Bañuls, and J. I. Cirac, Algorithms for quantum simulation at finite energies, *PRX Quantum* **2**, 020321 (2021).
- [74] Y. Yang, J. I. Cirac, and M. C. Bañuls, Classical algorithms for many-body quantum systems at finite energies, *Phys. Rev. B* **106**, 024307 (2022).
- [75] A. Schuckert, A. Bohrdt, E. Crane, and M. Knap, Probing finite-temperature observables in quantum simulators of spin systems with short-time dynamics, *Phys. Rev. B* **107**, L140410 (2023).
- [76] K. Ghanem, A. Schuckert, and H. Dreyer, Robust Extraction of Thermal Observables from State Sampling and Real-Time Dynamics on Quantum Computers, *Quantum* **7**, 1163 (2023).
- [77] E. Knill and R. Laflamme, On the power of one bit of quantum information, *Phys. Rev. Lett.* **81**, 5672 (1998).
- [78] A. Datta, S. T. Flammia, and C. M. Caves, Entanglement and the power of one qubit, *Phys. Rev. A* **72**, 042316 (2005).
- [79] D. Shepherd, Computation with unitaries and one pure qubit (2006), [arXiv:quant-ph/0608132](https://arxiv.org/abs/quant-ph/0608132) [quant-ph].
- [80] P. W. Shor and S. P. Jordan, Estimating Jones polynomials is a complete problem for one clean qubit, *Quant. Inf. Comput.* **8**, 0681 (2008).
- [81] F. G. S. L. Brandão, Entanglement Theory and the Quantum Simulation of Many-Body Physics, PhD thesis, Imperial College of Science, Technology and Medicine (2008), [arXiv:0810.0026](https://arxiv.org/abs/0810.0026).
- [82] A. N. Chowdhury, R. D. Somma, and Y. b. u. Subaşlı, Computing partition functions in the one-clean-qubit model, *Phys. Rev. A* **103**, 032422 (2021).
- [83] *System Model H1 Powered by Honeywell*, accessed on January 18th, 2024.
- [84] S. Sivarajah, S. Dilkes, A. Cowtan, W. Simmons, A. Edgington, and R. Duncan, T|ket): A retargetable compiler for NISQ devices, *Quantum Science and Technology* **6**, 014003 (2020), [arxiv:2003.10611](https://arxiv.org/abs/2003.10611).
- [85] T. Proctor, K. Rudinger, K. Young, E. Nielsen, and R. Blume-Kohout, Measuring the capabilities of quantum computers, *Nature Phys.* **18**, 75 (2022).
- [86] C. H. Baldwin, K. Mayer, N. C. Brown, C. Ryan-Anderson, and D. Hayes, Re-examining the quantum volume test: Ideal distributions, compiler optimizations, confidence intervals, and scalable resource estimations, *Quantum* **6**, 707 (2022).
- [87] F. Arute, K. Arya, R. Babbush, D. Bacon, J. C. Bardin, R. Barends, R. Biswas, S. Boixo, F. G. S. L. Brandao, D. A. Buell, B. Burkett, Y. Chen, Z. Chen, B. Chiaro, R. Collins, W. Courtney, A. Dunsworth, E. Farhi, B. Foxen, A. Fowler, C. Gidney, M. Giustina, R. Graff, K. Guerin, S. Habegger, M. P. Harrigan, M. J. Hartmann, A. Ho, M. Hoffmann, T. Huang, T. S. Humble, S. V. Isakov, E. Jeffrey, Z. Jiang, D. Kafri, K. Kechedzhi, J. Kelly, P. V. Klimov, S. Knysh, A. Korotkov, F. Kostritsa, D. Landhuis, M. Lindmark, E. Lucero, D. Lyakh, S. Mandrà, J. R. McClean, M. McEwen, A. Megrant, X. Mi, K. Michielsen, M. Mohseni, J. Mutus, O. Naaman, M. Neeley, C. Neill, M. Y. Niu, E. Ostby, A. Petukhov, J. C. Platt, C. Quintana, E. G. Rieffel, P. Roushan, N. C. Rubin, D. Sank, K. J. Satzinger, V. Smelyan-

- skiy, K. J. Sung, M. D. Trevithick, A. Vainsencher, B. Villalonga, T. White, Z. J. Yao, P. Yeh, A. Zalcman, H. Neven, and J. M. Martinis, Quantum supremacy using a programmable superconducting processor, *Nature* **574**, 505 (2019).
- [88] A. M. Dalzell, N. Hunter-Jones, and F. G. S. L. Brandão, Random quantum circuits transform local noise into global white noise (2021), [arXiv:2111.14907 \[quant-ph\]](https://arxiv.org/abs/2111.14907).
- [89] A. Summer, C. Chiaracane, M. T. Mitchison, and J. Goold, Calculating the many-body density of states on a digital quantum computer, *Phys. Rev. Res.* **6**, 013106 (2024).
- [90] K. Hémerly, K. Ghanem, E. Crane, S. L. Campbell, J. M. Dreiling, C. Figgatt, C. Foltz, J. P. Gaebler, J. Johansen, M. Mills, S. A. Moses, J. M. Pino, A. Ransford, M. Rowe, P. Siegfried, R. P. Stutz, H. Dreyer, A. Schuckert, and R. Nigmatullin, Measuring the loschmidt amplitude for finite-energy properties of the fermi-hubbard model on an ion-trap quantum computer (2023), [arXiv:2309.10552 \[quant-ph\]](https://arxiv.org/abs/2309.10552).
- [91] S. Sachdev and J. Ye, Gapless spin-fluid ground state in a random quantum heisenberg magnet, *Phys. Rev. Lett.* **70**, 3339 (1993).
- [92] A simple model of quantum holography, <http://online.kitp.ucsb.edu/online/entangled15/kitaev/> and <http://online.kitp.ucsb.edu/online/entangled15/kitaev2/>, Talks at KITP, April 7, 2015 and May 27, 2015.
- [93] J. Maldacena and D. Stanford, Remarks on the Sachdev-Ye-Kitaev model, *Phys. Rev. D* **94**, 106002 (2016), [arXiv:1604.07818 \[hep-th\]](https://arxiv.org/abs/1604.07818).
- [94] K. Seki, Y. Kikuchi, T. Hayata, and S. Yunoki, Research data supporting "Simulating Floquet scrambling circuits on trapped-ion quantum computers" (2024), <https://zenodo.org/records/11202425>.
- [95] S. Goto, R. Kaneko, and I. Danshita, Matrix product state approach for a quantum system at finite temperatures using random phases and Trotter gates, *Phys. Rev. B* **104**, 045133 (2021).
- [96] S. Goto, R. Kaneko, and I. Danshita, Evaluating thermal expectation values by almost ideal sampling with trotter gates, *Phys. Rev. B* **107**, 024307 (2023).
- [97] T. Iitaka, *Random Phase Product State for Canonical Ensemble* (2020).
- [98] H. De Raedt, F. Jin, D. Willsch, M. Willsch, N. Yoshioka, N. Ito, S. Yuan, and K. Michielsen, Massively parallel quantum computer simulator, eleven years later, *Computer Physics Communications* **237**, 47 (2019).
- [99] O. Watts, Y. Kikuchi, and L. Coopmans, Quantum Semidefinite Programming with Thermal Pure Quantum States (2023), [arXiv:2310.07774 \[quant-ph\]](https://arxiv.org/abs/2310.07774).
- [100] M. Horodecki, P. Horodecki, and R. Horodecki, General teleportation channel, singlet fraction, and quasidistillation, *Phys. Rev. A* **60**, 1888 (1999), [arXiv:quant-ph/9807091](https://arxiv.org/abs/quant-ph/9807091).
- [101] M. A. Nielsen, A simple formula for the average gate fidelity of a quantum dynamical operation, *Physics Letters A* **303**, 249 (2002).

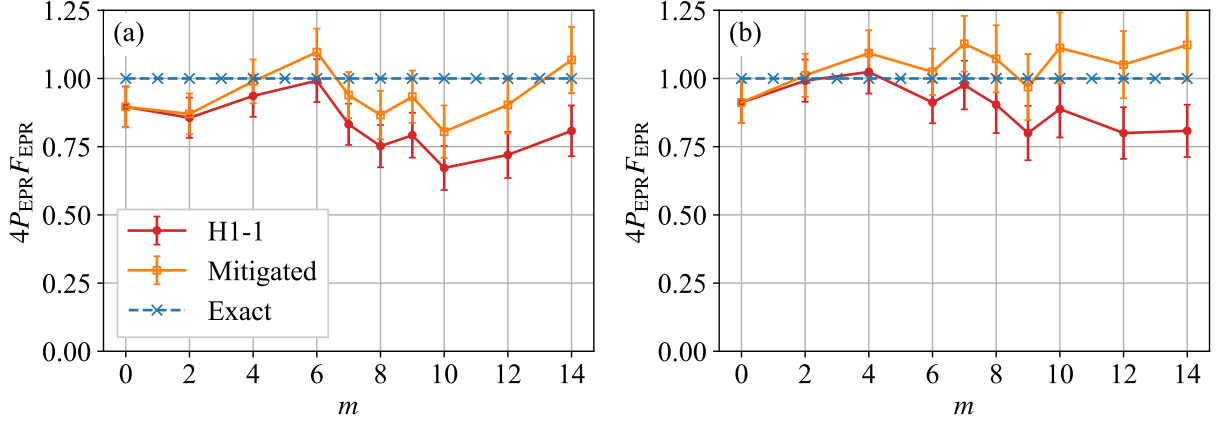


FIG. 10. The product of the post-selection probability P_{EPR} and the recovery fidelity F_{EPR} , multiplied by $d_A^2 = 4$, for (a) $JT = 1.3$ and (b) $JT = \pi/2$. These results correspond to those shown in Fig. 4.

Appendix A: Error mitigation

1. Hayden-Preskill recovery protocol

To model the noise effect in the HPR protocol, we consider a depolarizing channel \mathcal{D}_U acting on the unitary operator U , which acts on an N -qubit input state ρ as follows:

$$\mathcal{D}_U[\rho] = fU\rho U^\dagger + (1-f)\frac{I^{\otimes N}}{d}, \quad (\text{A1})$$

where $d = 2^N$ and $1-f$ represents the depolarizing error rate associated with the noisy application of U . By substituting the unitary U with the corresponding channel \mathcal{D}_U , we can express the post-selection probability $P_{\text{EPR}}^{\mathcal{D}}$ and the recovery fidelity $F_{\text{EPR}}^{\mathcal{D}}$ of \mathcal{D}_U using the ideal values P_{EPR} and F_{EPR} as follows:

$$P_{\text{EPR}}^{\mathcal{D}} = f^2 P_{\text{EPR}} + \frac{1-f^2}{d_D^2} \quad (\text{A2})$$

and

$$F_{\text{EPR}}^{\mathcal{D}} = \frac{1}{d_A^2 P_{\text{EPR}}^{\mathcal{D}}} \left[f^2 + \frac{1-f^2}{d_D^2} \right] = \frac{f^2 + d_D^{-2}(1-f^2)}{f^2/F_{\text{EPR}} + d_A^2 d_D^{-2}(1-f^2)}, \quad (\text{A3})$$

respectively [30]. Assuming that the results $P_{\text{EPR}}^{(\text{noisy})}$ and $F_{\text{EPR}}^{(\text{noisy})}$ obtained from noisy experiments are approximated by $P_{\text{EPR}}^{\mathcal{D}}$ and $F_{\text{EPR}}^{\mathcal{D}}$, we calculate the mitigated quantities $P_{\text{EPR}}^{(\text{mit})}$ and $F_{\text{EPR}}^{(\text{mit})}$ as given in Eqs. (22) and (23), respectively. Those mitigated quantities are shown along with the raw data in Fig. 4.

Noting that

$$d_A^2 P_{\text{EPR}}^{\mathcal{D}} F_{\text{EPR}}^{\mathcal{D}} = f^2 + \frac{1-f^2}{d_D^2}, \quad (\text{A4})$$

which is 1 in the absence of depolarizing noise as in Eq. (9), we can extract the strength of the noise by

$$d_A^2 P_{\text{EPR}}^{(\text{noisy})} F_{\text{EPR}}^{(\text{noisy})}. \quad (\text{A5})$$

Figure 10 shows $4P_{\text{EPR}}F_{\text{EPR}}$ obtained from the HPR protocol experiment with $d_A = 2$ using the Quantinuum H1-1 system, corresponding to the results shown in Fig. 4. Despite the presence of large statistical errors, we can find that $4P_{\text{EPR}}^{(\text{noisy})}F_{\text{EPR}}^{(\text{noisy})}$ tends to deviate from 1 as m increases.

2. Interferometric protocol for OTOCs

To mitigate the noise effect, following Refs. [8, 41], we calculate the normalized OTOC as

$$\frac{\langle 0^N | U X_n U^\dagger Z_1 U X_n U^\dagger | 0^N \rangle}{\langle 0^N | U I_n U^\dagger Z_1 U I_n U^\dagger | 0^N \rangle}. \quad (\text{A6})$$

where $U = (U_F)^m$ describes the unitary dynamics of the system [see Eq. (24)], and the denominator takes the value 1 in the absence of errors.

To analyze the behavior of the normalized OTOC in the presence of depolarizing noise, modeled by Eq. (A1), we compute the numerator and denominator with U replaced by \mathcal{D}_U in the circuit shown in Fig. 3, yielding respectively

$$\begin{aligned} \langle 0^N | U X_n U^\dagger Z_1 U X_n U^\dagger | 0^N \rangle^{\mathcal{D}} &= f^2 \langle 0^N | U X_n U^\dagger Z_1 U X_n U^\dagger | 0^N \rangle, \\ \langle 0^N | U I_n U^\dagger Z_1 U I_n U^\dagger | 0^N \rangle^{\mathcal{D}} &= f^2 \langle 0^N | U I_n U^\dagger Z_1 U I_n U^\dagger | 0^N \rangle = f^2. \end{aligned} \quad (\text{A7})$$

Thus, their ratio provides the OTOC without the depolarizing noise, $\langle 0^N | U X_n U^\dagger Z_1 U X_n U^\dagger | 0^N \rangle$.

Appendix B: Classical numerical results of OTOCs

Figure 11 shows the results of the operator-averaged OTOCs given by

$$\frac{1}{4^{N_A+N_D}} \sum_{O=\{I,X,Y,Z\}} \sum_{\bar{O}=\{I,X,Y,Z\}} \langle 0^N | (U_F)^{\dagger m} O_n (U_F)^m \bar{O}_1 (U_F)^{\dagger m} O_n (U_F)^m \bar{O}_1 | 0^N \rangle, \quad (\text{B1})$$

for the kicked Ising model with $N = 20$ spins under open boundary conditions, calculated classically for various JT values. Similar to Figs. 6 and 7, the other parameters are fixed to $B_X/J = \pi/2$ and $B_Z/J = 1.3$, with the subsystem sizes set as $N_A = 1$ and $N_D = 1$. Here, subsystem A on which operator \bar{O} acts remains fixed at one of the edges of the one-dimensional system, while the location n of subsystem D on which operator O acts is varied. We confirm that at $JT = \pi/2$, corresponding to the dual unitary point, the Floquet evolution induces the most rapid and pronounced decay of OTOCs among all cases shown in Fig. 11.

Figure 12 shows the same results but under periodic boundary conditions. The boundary effect approximately reduces the necessary number of Floquet cycles for complete system scrambling by half compared to the cases of open boundary conditions. Other than this point, we observe essentially the same results.

Appendix C: Statistical errors of normalized trace estimation

In this Appendix, we analyze how well the scrambled state approximates a state 2-design. To this end, we first show that the ensemble

$$\Psi = \{(U_F)^m |\psi_0\rangle \mid m \in \mathbb{N}, m_{\min} \leq m < m_{\max}\} \quad (\text{C1})$$

behaves like a state 2-design by numerically calculating the variance of Loschmidt amplitude $\mathcal{L}(t)$ in Eq. (17). We then provide justification for employing a single state sampled from the ensemble in Eq. (C1) to accurately estimate the normalized trace $\text{Tr}[\mathcal{U}(t)]/d$, where $\mathcal{U}(t)$ is a time-evolution operator of the system and d is the dimension of the corresponding Hilbert space.

Throughout this appendix, we denote the expectation value and sample mean by $\mathbb{E}[\cdot]$ and $\mathbb{E}'[\cdot]$, respectively, while $\text{Var}[\cdot]$ and $\text{Var}'[\cdot]$ represent the corresponding variances. To avoid shot noise, we employ classical simulations in this appendix and concentrate on the statistical properties of Floquet scrambled states. The numerical results presented here are obtained using the Floquet circuit, with a single Floquet cycle described by U_F as in Eq. (3), where the parameters are set to $B_z/J = 1$, $B_x/J = 1.3$, and $JT = \pi/2$. The time-evolution operator $\mathcal{U}(t)$ in the Loschmidt amplitude $\mathcal{L}(t)$ corresponds to the one-dimensional Heisenberg model \mathcal{H}_{XXX} under periodic boundary conditions, as defined in Eq. (25). In this section, we treat the time-evolution operator $\mathcal{U}(t)$ numerically exactly, instead of employing the single Trotter step approximation as described in Eq. (26)

1. Scrambling circuits form an approximate state 2-design

Figure 13(a) shows the Loschmidt amplitude $\mathcal{L}_m(t) = \langle \psi_0 | (U_F^\dagger)^m \mathcal{U}(t) (U_F)^m | \psi_0 \rangle$ averaged over states in the ensemble Ψ in Eq. (C1), i.e.,

$$\mathbb{E}_{\psi \sim \Psi}[\mathcal{L}(t)] := \frac{1}{M} \sum_{m=m_{\min}}^{m_{\max}-1} \mathcal{L}_m(t), \quad (\text{C2})$$

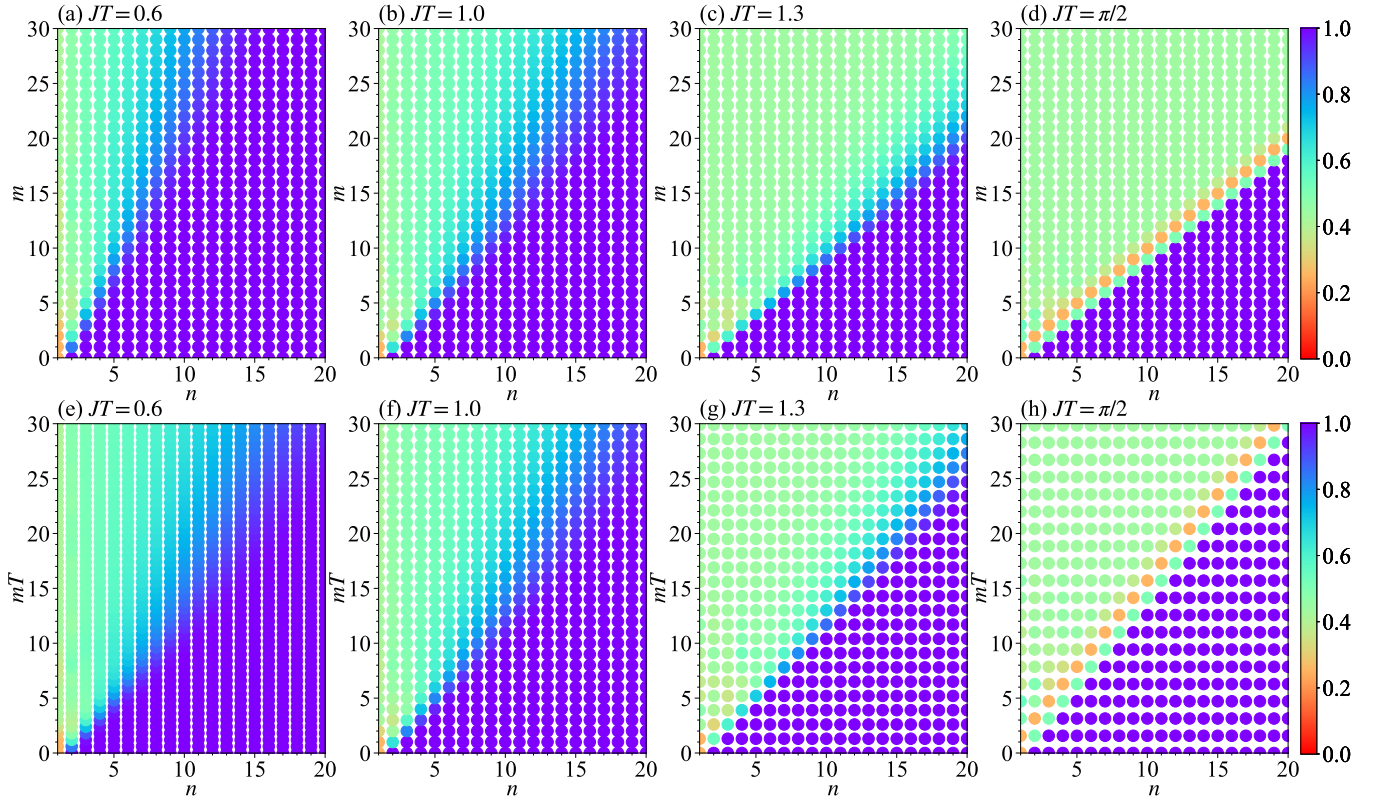


FIG. 11. (a-d) Operator-averaged OTOCs, defined in Eq. (B1), as a function of the position n of the butterfly operator and the number m of Floquet cycles, calculated classically for different JT values. The system consists of 20 spins under open boundary conditions. (e-h) Same as (a-d) but as a function of the evolution time mT , instead of the number of cycles m , in the vertical axis.

for $N = 20$. Here, $M = m_{\max} - m_{\min}$ is the number of states in ensemble Ψ and we set $m_{\min} = 10$ and $m_{\max} = 200$. We choose $m_{\min} = N/2 = 10$ to ensure that the Floquet states are sufficiently scrambled, while $m_{\max} = 200$ is selected to obtain nearly converged results for the standard deviation. For ensemble Ψ to approximate a state 2-design, M must be sufficiently large so that it contains samples whose time intervals are longer than the scrambling time. However, it should be noted that obtaining converged results for the mean of Loschmidt amplitude requires only a small number M of samples or even a single sample. The initial state $|\psi_0\rangle$ is fixed to a product state of the form $|\psi_0\rangle = \prod_{i=1}^N e^{-i\phi_i Y_i/2} |0^N\rangle$, where site-dependent angles $\{\phi_i\}_{i=1}^N$ are chosen randomly. As shown in Fig. 13(a), the ensemble average in Eq. (C2) coincides with the normalized trace of the time evolution operator, $\text{Tr}[\mathcal{U}(t)]/d$, within statistical errors, where $d = 2^N$ is the dimension of the Hilbert space.

Figure 13(b) shows the standard deviations of the real and imaginary parts of the Loschmidt amplitude, denoted as $\sigma_{\text{Re}\mathcal{L}(t)} := \sqrt{\text{Var}_{\psi \sim \Psi}[\text{Re}\mathcal{L}(t)]}$ and $\sigma_{\text{Im}\mathcal{L}(t)} := \sqrt{\text{Var}_{\psi \sim \Psi}[\text{Im}\mathcal{L}(t)]}$, respectively. They are associated with the variances

$$\text{Var}_{\psi \sim \Psi}[\text{Re}\mathcal{L}(t)] = \mathbb{E}_{\psi \sim \Psi}[\text{Re}\mathcal{L}(t)^2] - (\mathbb{E}_{\psi \sim \Psi}[\text{Re}\mathcal{L}(t)])^2 \quad (\text{C3})$$

and

$$\text{Var}_{\psi \sim \Psi}[\text{Im}\mathcal{L}(t)] = \mathbb{E}_{\psi \sim \Psi}[\text{Im}\mathcal{L}(t)^2] - (\mathbb{E}_{\psi \sim \Psi}[\text{Im}\mathcal{L}(t)])^2. \quad (\text{C4})$$

Additionally, Fig. 13(b) shows the standard deviation of the Loschmidt amplitude itself, denoted as $\sigma_{\mathcal{L}(t)} := \sqrt{\text{Var}_{\psi \sim \Psi}[\mathcal{L}(t)]}$, with the variance $\text{Var}_{\psi \sim \Psi}[\mathcal{L}(t)]$ calculated as the sum of the variances of its real and imaginary parts:

$$\text{Var}_{\psi \sim \Psi}[\mathcal{L}(t)] = \text{Var}_{\psi \sim \Psi}[\text{Re}\mathcal{L}(t)] + \text{Var}_{\psi \sim \Psi}[\text{Im}\mathcal{L}(t)]. \quad (\text{C5})$$

Although mostly invisible because they are smaller than the size of symbols, the error bars in Fig. 13(a) represent the standard deviations of the mean, calculated as $\sqrt{\text{Var}_{\psi \sim \Psi}[\text{Re}\mathcal{L}(t)]/M}$ and $\sqrt{\text{Var}_{\psi \sim \Psi}[\text{Im}\mathcal{L}(t)]/M}$ for the real and imaginary parts of the Loschmidt amplitude, respectively.

To gain insights into the numerical results of the standard deviations, let us consider the case where Haar random states are used instead of $|\psi(m)\rangle = \{(U_F)^m |\psi_0\rangle$. In this case, the variance $\text{Var}_{\psi \sim \text{Haar}}[\mathcal{L}(t)]$ is given by

$$\text{Var}_{\psi \sim \text{Haar}}[\mathcal{L}(t)] = \mathbb{E}_{\psi \sim \text{Haar}}[\mathcal{L}(t)^2] - (\mathbb{E}_{\psi \sim \text{Haar}}[\mathcal{L}(t)])^2 = \frac{1 - \text{SFF}(t)}{d + 1}, \quad (\text{C6})$$

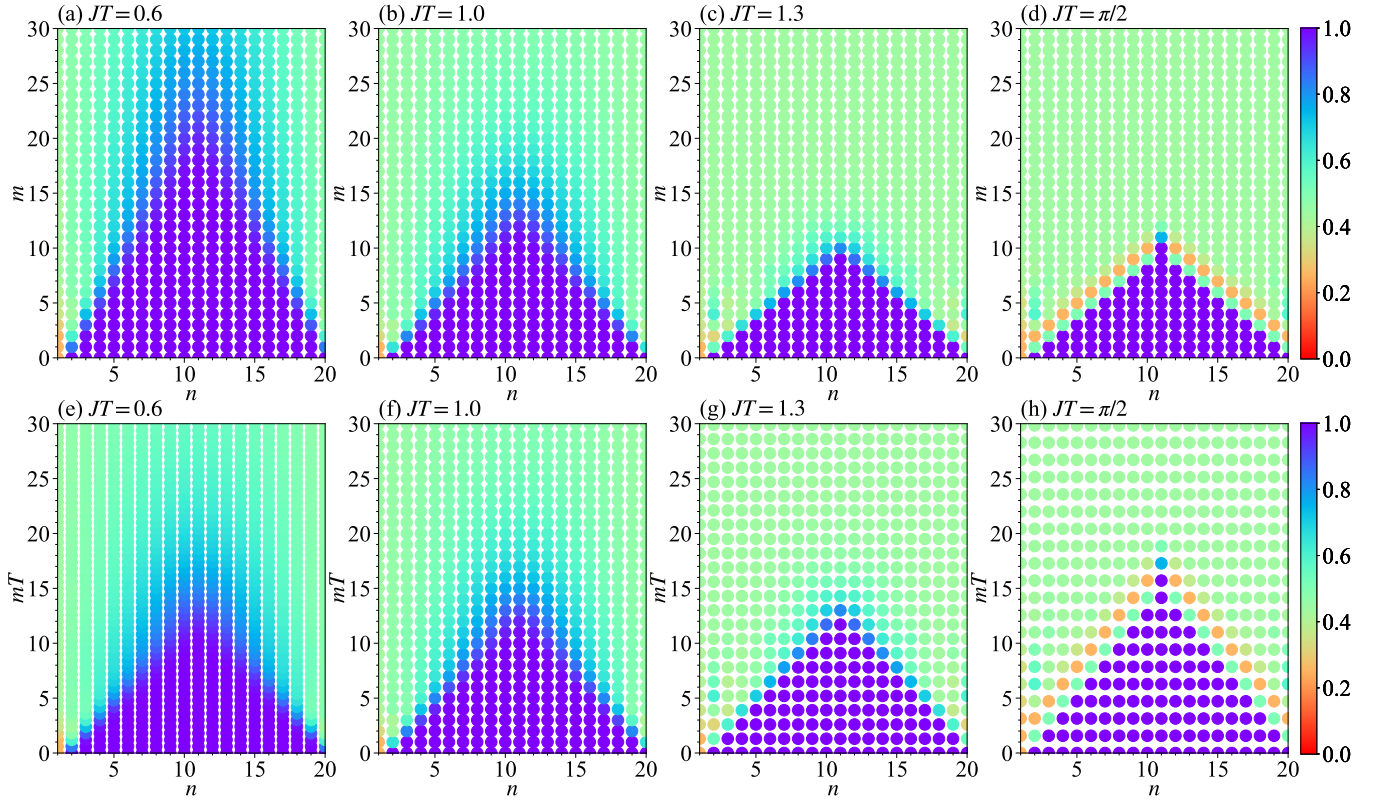


FIG. 12. Same as Fig. 11 but for periodic boundary conditions.

where $\text{SFF}(t) := |\text{Tr}[\mathcal{U}(t)]|^2/d^2$ is the spectral form factor. Since $0 \leq \text{SFF}(t) \leq 1$, the standard deviation $\sigma_{\text{Haar}}(t) = \sqrt{\text{Var}_{\psi \sim \text{Haar}}[\mathcal{L}(t)]}$ is bounded as $0 \leq \sigma_{\text{Haar}}(t) \leq 1/\sqrt{d+1}$. Moreover, the spectral form factor decays in time to zero at $t \sim \sigma_{\mathcal{H}}^{-1}$, where $\sigma_{\mathcal{H}}$ is defined in Eq. (29). The decay of $\text{SFF}(t)$ in the early time $t \lesssim \sigma_{\mathcal{H}}^{-1}$ can be understood by noticing that $\text{SFF}(t)$ is proportional to the absolute square of the Fourier transform of the density of states, which has an approximate energy extent of $\sigma_{\mathcal{H}}$. Thus, the standard deviation $\sigma_{\text{Haar}}(t)$ can be approximated as $\sigma_{\text{Haar}}(t) \approx 1/\sqrt{d+1}$ for $t \gg \sigma_{\mathcal{H}}^{-1}$ [see Fig. 13(b)].

As shown in Fig. 13(b), the standard deviations of the real and imaginary parts, $\sigma_{\text{Re}\mathcal{L}(t)}$ and $\sigma_{\text{Im}\mathcal{L}(t)}$, respectively, align with $\sigma_{\text{Haar}}(t)/\sqrt{2}$. Consequently, the standard deviation $\sigma_{\mathcal{L}(t)}$ agrees with the corresponding Haar value $\sigma_{\text{Haar}}(t)$. This agreement between $\sigma_{\mathcal{L}(t)}$ and $\sigma_{\text{Haar}}(t)$ suggests that the ensemble Ψ approximates a state 2-design.

2. Accurate estimate of normalized trace with a single scrambled state

In the previous subsection, we numerically confirmed that the ensemble Ψ in Eq. (C1) behaves like an approximate state 2-design. Here, we justify that a single state $(U_{\text{F}})^m |\psi_0\rangle$ with a sufficiently large m (specifically, here we consider $m \gtrsim N/2$ for one-dimensional systems under periodic boundary conditions) suffices to estimate the normalized trace $\text{Tr}[\mathcal{U}(t)]/d$ accurately. For the sake of numerical study, we randomly sample initial product states $|\psi_0\rangle$ with a fixed number m of Floquet cycles. As described in Sec. IV C, we define our Floquet scrambled states as $|\psi_r\rangle = (U_{\text{F}})^m |\psi_0^{(r)}\rangle$ with the initial product state $|\psi_0^{(r)}\rangle = \prod_{i=1}^N e^{-i\phi_{i,r} Y_i/2} |0^N\rangle$, where $\{\phi_{i,r}\}_{i=1}^N$ is the r th set of independent random angles. We should note here that the random initialization in $|\psi_0^{(r)}\rangle$ corresponds to the average over a tensor product of single-qubit Haar random unitaries, which by itself does not form a state 2-design over an N -qubit system (also see Fig. 16).

Figures 14(a,b) show the Loschmidt amplitude $\mathcal{L}_r(t) = \langle \psi_r | \mathcal{U}(t) | \psi_r \rangle$ averaged over R distinct random initializations, i.e.,

$$\mathbb{E}'_{\psi \sim \Psi_m}[\mathcal{L}(t)] := \frac{1}{R} \sum_{r=1}^R \mathcal{L}_r(t), \quad (\text{C7})$$

for the one-dimensional Heisenberg model \mathcal{H}_{XX} with $N = 20$ and 24 sites, respectively. Here, $\Psi_m = \{(U_{\text{F}})^m \prod_{i=1}^N e^{-i\phi_{i,r} Y_i/2} |0^N\rangle \mid r = 1, \dots, R\}$ represents an ensemble of states with a fixed number m of Floquet cycles. We set the number of Floquet cycles to

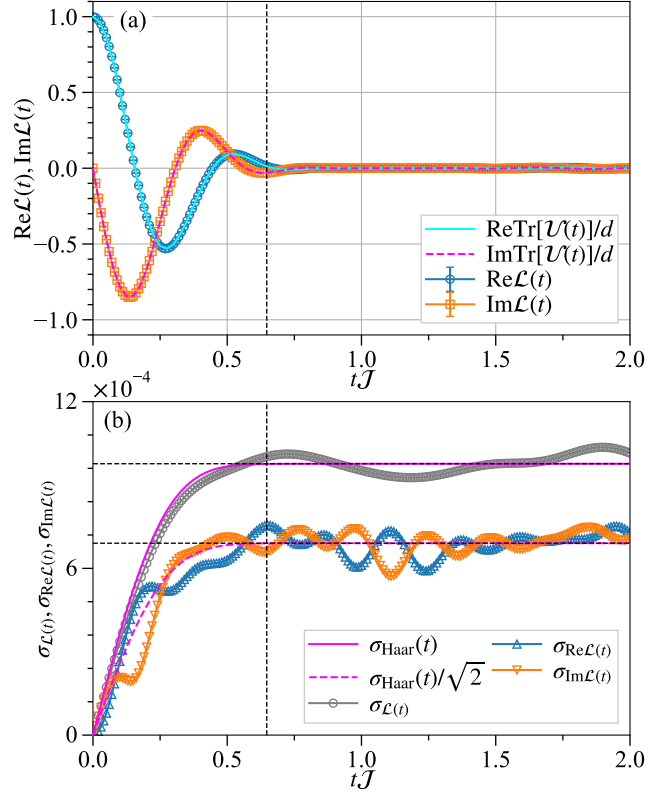


FIG. 13. (a) Averaged real and imaginary parts of the Loschmidt amplitude, $\mathbb{E}_{\psi \sim \Psi}[\text{Re}\mathcal{L}(t)]$ and $\mathbb{E}_{\psi \sim \Psi}[\text{Im}\mathcal{L}(t)]$, denoted by circles and squares, respectively, for the one-dimensional Heisenberg model \mathcal{H}_{XXX} with $N = 20$ sites under periodic boundary conditions. The average is taken over the ensemble Ψ in Eq. (C1). For comparison, the exact results of $\text{ReTr}[\mathcal{U}(t)]/d$ and $\text{ImTr}[\mathcal{U}(t)]/d$ are also shown by solid and dashed curves, respectively. (b) Standard deviations of the Loschmidt amplitude, $\sigma_{\mathcal{L}(t)}$, and its real and imaginary parts, $\sigma_{\text{Re}\mathcal{L}(t)}$ and $\sigma_{\text{Im}\mathcal{L}(t)}$, respectively, corresponding to the results shown in (a). The solid and dashed curves indicate the standard deviation $\sigma_{\text{Haar}}(t)$ and $\sigma_{\text{Haar}}(t)/\sqrt{2}$, respectively, calculated for Haar random states. The two dashed horizontal lines indicate $1/\sqrt{d+1}$ and $1/\sqrt{2(d+1)}$. The dashed vertical lines in (a) and (b) indicate $t = \sigma^{-1}$, where σ is defined in Eq. (28).

$m = N/2$, while $R = 100$ is chosen to achieve nearly converged results for the standard deviation. However, only a small number R of samples is required to obtain converged results for the Loschmidt amplitude. As expected, the statistical average coincides with the normalized trace of the time evolution operator within statistical errors, i.e., $\mathbb{E}'_{\psi \sim \Psi_m}[\mathcal{L}(t)] \approx \text{Tr}[\mathcal{U}(t)]/d$.

Figures 14(c,d) show the standard deviations of the real and the imaginary parts of the Loschmidt amplitude, denoted as $\sigma_{\text{Re}\mathcal{L}(t)} := \sqrt{\text{Var}'_{\psi}[\text{Re}\mathcal{L}(t)]}$ and $\sigma_{\text{Im}\mathcal{L}(t)} := \sqrt{\text{Var}'_{\psi}[\text{Im}\mathcal{L}(t)]}$, respectively. They are associated to the variances

$$\text{Var}'_{\psi \sim \Psi_m}[\text{Re}\mathcal{L}(t)] = \mathbb{E}'_{\psi \sim \Psi_m}[\text{Re}\mathcal{L}(t)^2] - (\mathbb{E}'_{\psi \sim \Psi_m}[\text{Re}\mathcal{L}(t)])^2 \quad (\text{C8})$$

and

$$\text{Var}'_{\psi \sim \Psi_m}[\text{Im}\mathcal{L}(t)] = \mathbb{E}'_{\psi \sim \Psi_m}[\text{Im}\mathcal{L}(t)^2] - (\mathbb{E}'_{\psi \sim \Psi_m}[\text{Im}\mathcal{L}(t)])^2. \quad (\text{C9})$$

Additionally, Figs. 14(c,d) show the standard deviation of the Loschmidt amplitude, denoted as $\sigma_{\mathcal{L}(t)} := \sqrt{\text{Var}'_{\psi}[\mathcal{L}(t)]}$, with the variance $\text{Var}'_{\psi}[\mathcal{L}(t)]$ calculated as the sum of the variances of its real and imaginary parts:

$$\text{Var}'_{\psi \sim \Psi_m}[\mathcal{L}(t)] = \text{Var}'_{\psi \sim \Psi_m}[\text{Re}\mathcal{L}(t)] + \text{Var}'_{\psi \sim \Psi_m}[\text{Im}\mathcal{L}(t)]. \quad (\text{C10})$$

Although mostly invisible because they are smaller than the size of symbols, the error bars in Figs. 14(a,b) represent the standard deviations of the mean, calculated as $\sqrt{\text{Var}'_{\psi}[\text{Re}\mathcal{L}(t)]/R}$ and $\sqrt{\text{Var}'_{\psi}[\text{Im}\mathcal{L}(t)]/R}$ for the real and imaginary parts of the Loschmidt amplitude, respectively. As shown in Figs. 14(c,d), the standard deviation of the Loschmidt amplitude $\sigma_{\mathcal{L}(t)}$ aligns with $\sigma_{\text{Haar}}(t)$. Moreover, the standard deviations of the real and imaginary parts, $\sigma_{\text{Re}\mathcal{L}(t)}$ and $\sigma_{\text{Im}\mathcal{L}(t)}$, respectively, also closely follow $\sigma_{\text{Haar}}(t)/\sqrt{2}$.

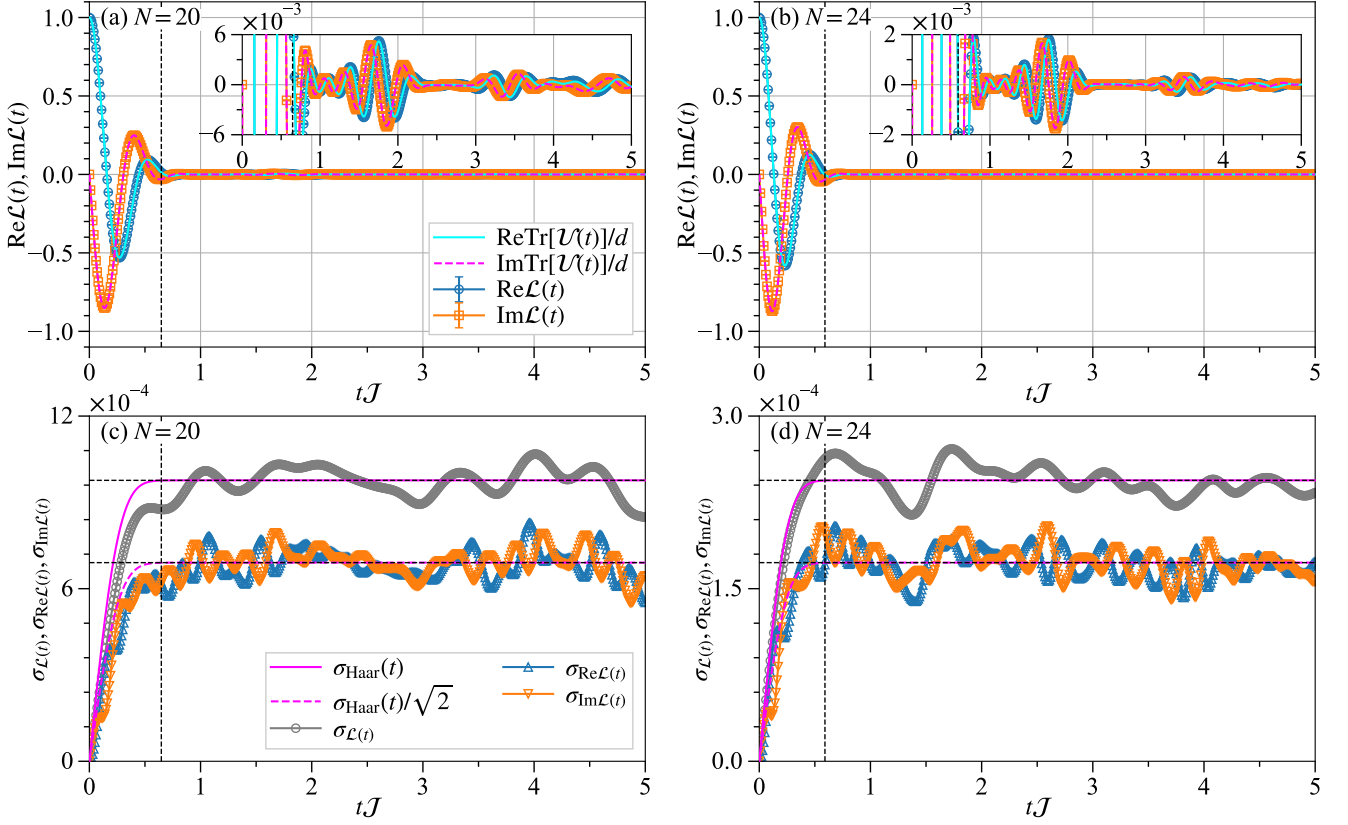


FIG. 14. (a,b) Sample-averaged real and imaginary parts of the Loschmidt amplitude, $\mathbb{E}'_{\Psi_m}[\text{Re}\mathcal{L}(t)]$ and $\mathbb{E}'_{\Psi_m}[\text{Im}\mathcal{L}(t)^2]$, denoted by circles and squares, respectively, for the one-dimensional Heisenberg model \mathcal{H}_{XX} with $N = 20$ and 24 sites under periodic boundary conditions. The sample average is taken over the ensemble Ψ_m with the number of Floquet cycles $m = N/2$. For comparison, the exact results of $\text{ReTr}[\mathcal{U}(t)]/d$ and $\text{ImTr}[\mathcal{U}(t)]/d$ are also shown by solid and dashed curves, respectively, where $d = 2^N$ is the dimension of the Hilbert space. The insets show an enlarged view around zero. (c,d) Sample-averaged standard deviations of the Loschmidt amplitude, $\sigma_{\mathcal{L}(t)}$, and its real and imaginary parts, $\sigma_{\text{Re}\mathcal{L}(t)}$ and $\sigma_{\text{Im}\mathcal{L}(t)}$, respectively, corresponding to the results shown in (a,b). The solid and dashed curves indicate the standard deviation $\sigma_{\text{Haar}}(t)$ and $\sigma_{\text{Haar}}(t)/\sqrt{2}$, respectively, calculated for Haar random states. The two dashed horizontal lines indicate $1/\sqrt{d+1}$ and $1/\sqrt{2(d+1)}$. The dashed vertical lines in (a-d) indicate $t = \sigma^{-1}$, where σ is defined in Eq. (28).

Figure 15 shows the system size dependence of the standard deviations $\sigma_{\mathcal{L}(t)}$, $\sigma_{\text{Re}\mathcal{L}(t)}$, and $\sigma_{\text{Im}\mathcal{L}(t)}$ averaged over time for $\sigma^{-1}\mathcal{J} < t\mathcal{J} \leq 5$, where σ is defined in Eq. (28). Here, these standard deviations are evaluated over the ensemble Ψ_m with the number of Floquet cycles $m = N/2$, as shown in Figs. 14(c,d) for $N = 20$ and 24 sites, respectively. The exponential decrease of the standard deviations with respect to N is clearly observed in Fig. 15.

Figure 16 shows the standard deviations $\sigma_{\mathcal{L}(t)}$ of the Loschmidt amplitude with various values of the Floquet cycles m in Ψ_m for $N = 20$ and 24 sites. The result for $m = 0$ corresponds to the standard deviation evaluated with respect to a set of the random product states $\{|\psi_0^{(r)}\rangle\} = \prod_{i=1}^N e^{-i\phi_{i,r}Y_i/2}|0^N\rangle_{r=1}^R$. As shown in Fig. 16, with increasing m , the standard deviation $\sigma_{\mathcal{L}(t)}$ approaches the Haar value $\sigma_{\text{Haar}}(t)$, and a good agreement is found for $m \gtrsim N/2$. This result, together with the scrambling dynamics of the OTOC shown in Fig. 12(d), suggests that the ensemble of states Ψ_m forms an approximate state 2-design for $m \gtrsim N/2$ under periodic boundary conditions.

The above result is consistent with the observations made in Refs. [95, 96], where they found that thermal expectation values can be efficiently evaluated using random-phase-product states [97] evolved by a Trotterized time evolution operator of a nonintegrable Hamiltonian, with Trotter cycles proportional to the system size. Their choice of a large Trotter time step implies dynamics resembling Floquet dynamics rather than Hamiltonian dynamics. Therefore, our result suggests that their observations can be attributed to Floquet scrambling of states behaving as an approximate state 2-design.

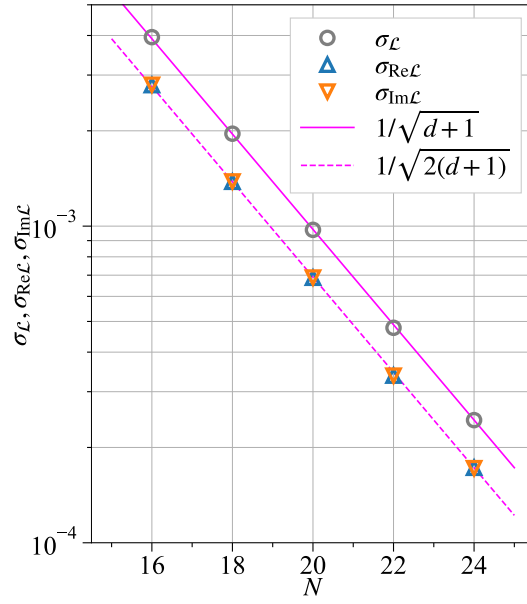


FIG. 15. Standard deviations of the Loschmidt amplitude, and its real and imaginary parts, $\sigma_{\mathcal{L}}$, $\sigma_{\text{Re}\mathcal{L}}$, and $\sigma_{\text{Im}\mathcal{L}}$, respectively, averaged over time for $\sigma^{-1}\mathcal{J} < t\mathcal{J} \leq 5$, plotted as a function of the system size N . Here, σ is defined in Eq. (28) and the number of Floquet circles in Ψ_m is $m = N/2$. The solid and dashed magenta lines indicate $1/\sqrt{d+1}$ and $1/\sqrt{2(d+1)}$, respectively, where $d = 2^N$ is the dimension of the Hilbert space.

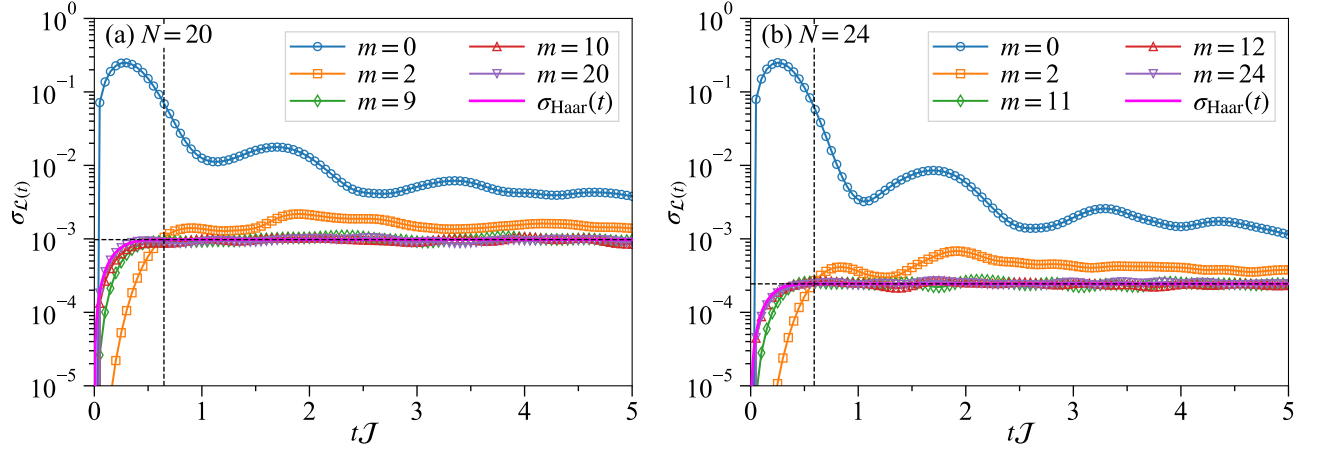


FIG. 16. Sample-averaged standard deviations $\sigma_{\mathcal{L}(t)}$ of the Loschmidt amplitude for the one-dimensional Heisenberg model \mathcal{H}_{XXX} with (a) $N = 20$ and (b) $N = 24$ sites under periodic boundary conditions are evaluated for various values of the Floquet cycles m in the ensemble Ψ_m . For comparison, the standard deviations evaluated for Haar random states, $\sigma_{\text{Haar}}(t)$, are also plotted by solid curves. The dashed horizontal lines and the dashed vertical lines indicate $\sigma_{\mathcal{L}(t)} = 1/\sqrt{d+1}$ and $t = \sigma^{-1}$, respectively, where $d = 2^N$ is the dimension of the Hilbert space and σ is defined in Eq. (28). Note that the results for $m = N/2$ are the same as those shown in Figs. 14(c,d).

3. Influence of shot noise on the normalized trace estimation

In the previous subsections, we assumed that the shot noise was absent, which is relevant for classical simulations or quantum simulations in the limit of the infinite number of shots. Now, we discuss the statistical errors of the Loschmidt amplitude in the presence of the shot noise, assuming that the number of shots N_{shots} is finite.

a. *Sampling over shots*

First, let us consider the shot noise when evaluating the Loschmidt amplitude, $\mathcal{L}(t) = \langle \psi | \mathcal{U}(t) | \psi \rangle$, for a fixed pure state $|\psi\rangle$. Using the Hadamard test, the Loschmidt amplitude is estimated as $\mathbb{E}'_{\text{shots}}[x_\psi] + i\mathbb{E}'_{\text{shots}}[y_\psi]$, where $\mathbb{E}'_{\text{shots}}[x_\psi]$ and $\mathbb{E}'_{\text{shots}}[y_\psi]$ represent the sample means of its real and imaginary parts, respectively, obtained from the measurement outcomes on the ancillary qubit, i.e.,

$$\mathbb{E}'_{\text{shots}}[x_\psi] := \frac{1}{N_{\text{shots}}} \sum_{c=1}^{N_{\text{shots}}} x_{\psi,c}, \quad \mathbb{E}'_{\text{shots}}[y_\psi] := \frac{1}{N_{\text{shots}}} \sum_{c=1}^{N_{\text{shots}}} y_{\psi,c}. \quad (\text{C11})$$

Here, $x_{\psi,c} \in \{+1, -1\}$ denotes the X -measurement outcome of the ancillary qubit for the c -th shot, and similarly $y_{\psi,c} \in \{+1, -1\}$ is the Y -measurement outcome. The sample variances of the real and imaginary parts due to the finite number of shots are given respectively by

$$\text{Var}'_{\text{shots}}[x_\psi] = 1 - (\mathbb{E}'_{\text{shots}}[x_\psi])^2, \quad \text{Var}'_{\text{shots}}[y_\psi] = 1 - (\mathbb{E}'_{\text{shots}}[y_\psi])^2. \quad (\text{C12})$$

The standard deviations of the means are then calculated as

$$\sigma_{\text{shots}}^{\text{mean}}[x_\psi] := \sqrt{\frac{\text{Var}'_{\text{shots}}[x_\psi]}{N_{\text{shots}}}}, \quad \sigma_{\text{shots}}^{\text{mean}}[y_\psi] := \sqrt{\frac{\text{Var}'_{\text{shots}}[y_\psi]}{N_{\text{shots}}}}. \quad (\text{C13})$$

b. *Sampling over states*

The above result is for a single pure state $|\psi\rangle$. Now, we extend this analysis to the average over R independent realizations of states $\{|\psi_r\rangle\}_{r=1}^R$. The corresponding estimator of the normalized trace is given by $\mathbb{E}'_\psi[\mathbb{E}'_{\text{shots}}[x_\psi]] + i\mathbb{E}'_\psi[\mathbb{E}'_{\text{shots}}[y_\psi]]$, where

$$\mathbb{E}'_\psi[\mathbb{E}'_{\text{shots}}[x_\psi]] := \frac{1}{R} \sum_{r=1}^R \mathbb{E}'_{\text{shots}}[x_{\psi_r}], \quad \mathbb{E}'_\psi[\mathbb{E}'_{\text{shots}}[y_\psi]] := \frac{1}{R} \sum_{r=1}^R \mathbb{E}'_{\text{shots}}[y_{\psi_r}]. \quad (\text{C14})$$

The sample variances of the real and imaginary parts due to the sampling over states $|\psi_r\rangle$ are given respectively by

$$\text{Var}'_\psi[\mathbb{E}'_{\text{shots}}[x_\psi]] := \mathbb{E}'_\psi[\mathbb{E}'_{\text{shots}}[x_\psi]^2] - (\mathbb{E}'_\psi[\mathbb{E}'_{\text{shots}}[x_\psi]])^2 \quad (\text{C15})$$

and

$$\text{Var}'_\psi[\mathbb{E}'_{\text{shots}}[y_\psi]] := \mathbb{E}'_\psi[\mathbb{E}'_{\text{shots}}[y_\psi]^2] - (\mathbb{E}'_\psi[\mathbb{E}'_{\text{shots}}[y_\psi]])^2. \quad (\text{C16})$$

The corresponding standard deviations of the mean due to the sampling over states are then calculated as

$$\sigma_\psi^{\text{mean}}[\mathbb{E}'_{\text{shots}}[x_\psi]] := \sqrt{\frac{\text{Var}'_\psi[\mathbb{E}'_{\text{shots}}[x_\psi]]}{R}}, \quad \sigma_\psi^{\text{mean}}[\mathbb{E}'_{\text{shots}}[y_\psi]] := \sqrt{\frac{\text{Var}'_\psi[\mathbb{E}'_{\text{shots}}[y_\psi]]}{R}}. \quad (\text{C17})$$

Here, we first average over shots and then states, to associate the result in the previous subsection with the present analysis. Alternatively, one could average over shots and states simultaneously: $\text{Var}'[x] := \mathbb{E}'_\psi[\mathbb{E}'_{\text{shots}}[x_\psi^2]] - (\mathbb{E}'_\psi[\mathbb{E}'_{\text{shots}}[x_\psi]])^2 = 1 - (\mathbb{E}'_\psi[\mathbb{E}'_{\text{shots}}[x_\psi]])^2$ with a similar expression for $\text{Var}'[y]$. Then, as discussed in the next subsection, one could readily find that the standard deviation of the mean is given by the right-hand side of Eq. (C24) assuming that the states are sampled from a state 2-design.

c. *Sampling over shots and states*

Recall that each sample mean $\mathbb{E}'_{\text{shots}}[x_\psi]$ for a given $|\psi\rangle$ has the standard deviation $\sigma_{\text{shots}}^{\text{mean}}[x_\psi] (\sim 1/\sqrt{N_{\text{shots}}})$ around the population mean. Therefore, the standard deviation of $\mathbb{E}'_\psi[\mathbb{E}'_{\text{shots}}[x_\psi]]$ should be described by both $\sigma_\psi^{\text{mean}}$ and $\sigma_{\text{shots}}^{\text{mean}}$ (the same applies to $\mathbb{E}'_\psi[\mathbb{E}'_{\text{shots}}[y_\psi]]$). From the error-propagation formula, the standard deviations of the means $\mathbb{E}'_\psi[\mathbb{E}'_{\text{shots}}[x_\psi]]$ and $\mathbb{E}'_\psi[\mathbb{E}'_{\text{shots}}[y_\psi]]$ are expressed respectively as

$$\sigma^{\text{mean}}[x] := \sqrt{(\sigma_\psi^{\text{mean}}[\mathbb{E}'_{\text{shots}}[x_\psi]])^2 + \frac{1}{R^2} \sum_{r=1}^R (\sigma_{\text{shots}}^{\text{mean}}[x_{\psi_r}])^2} \quad (\text{C18})$$

and

$$\sigma^{\text{mean}}[y] := \sqrt{\left(\sigma_{\psi}^{\text{mean}}[\mathbb{E}'_{\text{shots}}[y_{\psi}]]\right)^2 + \frac{1}{R^2} \sum_{r=1}^R \left(\sigma_{\text{shots}}^{\text{mean}}[y_{\psi_r}]\right)^2}. \quad (\text{C19})$$

d. Standard deviation of the mean in the presence of the shot noise assuming a state 2-design

To proceed further, we consider $\sigma^{\text{mean}}[x+iy] = \sqrt{(\sigma^{\text{mean}}[x])^2 + (\sigma^{\text{mean}}[y])^2}$ for simplicity. Additionally, we make the following replacements: $\mathbb{E}'_{\text{shots}}[x_{\psi}] \rightarrow \mathbb{E}_{\text{shots}}[x_{\psi}] = \text{Re} \langle \psi | U(t) | \psi \rangle$, $\mathbb{E}'_{\text{shots}}[y_{\psi}] \rightarrow \mathbb{E}_{\text{shots}}[y_{\psi}] = \text{Im} \langle \psi | U(t) | \psi \rangle$, and $\mathbb{E}'_{\psi}[\dots] \rightarrow \mathbb{E}_{\psi \sim 2\text{-design}}[\dots]$. Then, the variance due to the shots averaged over states is replaced with

$$\frac{1}{R^2} \sum_{r=1}^R \left(\sigma_{\text{shots}}^{\text{mean}}[x_{\psi_r} + iy_{\psi_r}]\right)^2 \rightarrow \frac{1}{RN_{\text{shots}}} \left(2 - \frac{1}{d+1} - \frac{d\text{SFF}(t)}{d+1}\right), \quad (\text{C20})$$

and the variance due to the sampling of states is replaced with

$$\left(\sigma_{\psi_r}^{\text{mean}}[\mathbb{E}'_{\text{shots}}[x_{\psi_r} + iy_{\psi_r}]]\right)^2 \rightarrow \frac{1 - \text{SFF}(t)}{R(d+1)}. \quad (\text{C21})$$

The standard deviation of the mean is then replaced with

$$\sigma^{\text{mean}}[x+iy] \rightarrow \sqrt{\frac{1 - \text{SFF}(t)}{R(d+1)} + \frac{1}{RN_{\text{shots}}} \left(2 - \frac{1}{d+1} - \frac{d\text{SFF}(t)}{d+1}\right)}. \quad (\text{C22})$$

Let us first consider a situation relevant to classical state-vector simulations where the output of the Loschmidt amplitude is given by a double-precision (single-precision) floating-point number with a relative error due to round-off of at most 2^{-53} (2^{-24}). Assuming $R = O(1)$ and requiring the shot noise to be no larger than this round-off error, the corresponding number of shots would be around $N_{\text{shots}} \sim 2^{106}$ (2^{48}). On the other hand, the classically tractable dimension of the Hilbert space is at most $d \sim 2^{48}$ [98]. Therefore, in most cases, classical state-vector simulations with double-precision arithmetic satisfy the relation $R \ll d \ll N_{\text{shots}}$. By taking the limit of $N_{\text{shots}} \rightarrow \infty$ with finite d and R , we obtain the result consistent with Eq. (C6) in the previous subsection:

$$\sigma^{\text{mean}}[x+iy] \xrightarrow{N_{\text{shots}} \rightarrow \infty} \sqrt{\frac{1 - \text{SFF}(t)}{R(d+1)}}. \quad (\text{C23})$$

Next, we consider a situation relevant to quantum computation, where the relation $R \ll N_{\text{shots}} \ll d$ holds. In this case, by taking the limit of $d \rightarrow \infty$ with finite N_{shots} and R , the standard deviation of the mean simplifies to

$$\sigma^{\text{mean}}[x+iy] \xrightarrow{d \rightarrow \infty} \sqrt{\frac{2 - \text{SFF}(t)}{RN_{\text{shots}}}}. \quad (\text{C24})$$

Thus, unless N_{shots} is as large as $O(d)$, the shot noise dominates σ^{mean} .

Appendix D: Error in microcanonical expectation value due to a state 2-design

In this Appendix, we shall prove the inequality stated in Eq. (13). We introduce a filter operator defined as

$$G_{\sigma}(E) := e^{-(E-H)^2/2\sigma^2}, \quad (\text{D1})$$

and examine a thermal state $\rho_{\sigma} = G_{\sigma}/\text{Tr}[G_{\sigma}]$ representing the microcanonical ensemble parametrized by the internal energy E and width σ . The thermal entropy is expressed as

$$S_{\sigma}(E) = \log \text{Tr}[G_{\sigma}(E)], \quad (\text{D2})$$

while the microcanonical expectation value of a Hermitian operator O is calculated by

$$\langle O \rangle = \text{Tr}[O\rho_{\sigma}]. \quad (\text{D3})$$

Here, we estimate the expectation value $\langle O \rangle$ using a state 2-design. Letting $|\psi\rangle$ be a state sampled from a state 2-design, we compute

$$\langle O \rangle^{(\text{est})} = \frac{\langle \psi | OG_\sigma | \psi \rangle}{\langle \psi | G_\sigma | \psi \rangle}. \quad (\text{D4})$$

We first prove that this gives an accurate estimator of $\langle O \rangle$ in Eq. (D3) with high probability. To this end, we show the mean-square error

$$\mathbb{E}_\psi [|\langle O \rangle^{(\text{est})} - \langle O \rangle|^2] = |\mathbb{E}_\psi [\langle O \rangle^{(\text{est})}] - \langle O \rangle|^2 + \text{Var}_\psi [\langle O \rangle^{(\text{est})}], \quad (\text{D5})$$

is exponentially small in the system size N and then we employ the Chebyshev inequality, as shown in Eq. (D26). Here, The first and second terms on the right-hand side in Eq. (D5) represent the squared bias and the statistical uncertainty, respectively.

Following Refs. [53, 57, 99], we introduce the quantities

$$f := \langle \psi | OG_\sigma(E) | \psi \rangle, \quad g := \langle \psi | G_\sigma(E) | \psi \rangle. \quad (\text{D6})$$

Upon averaging $|\psi\rangle$ over the state 2-design, we obtain

$$\mathbb{E}_\psi [f] = \frac{\text{Tr}[OG_\sigma]}{d}, \quad \mathbb{E}_\psi [g] = \frac{\text{Tr}[G_\sigma]}{d}, \quad (\text{D7})$$

along with the variances

$$\begin{aligned} \text{Var}_\psi [f] &= \mathbb{E}_\psi [|\langle \psi | OG_\sigma | \psi \rangle|^2] - |\mathbb{E}_\psi [\langle \psi | OG_\sigma | \psi \rangle]|^2 \\ &= \frac{\text{Tr}[O^\dagger OG_\sigma^2] + |\text{Tr}[OG_\sigma]|^2}{d(d+1)} - \frac{|\text{Tr}[OG_\sigma]|^2}{d^2} \leq \|O\|^2 (\text{Tr}[G_\sigma])^2 \frac{\text{Tr}[\rho_\sigma^2]}{d^2} \end{aligned} \quad (\text{D8})$$

and

$$\text{Var}_\psi [g] = \mathbb{E}_\psi [\langle \psi | G_\sigma | \psi \rangle^2] - (\mathbb{E}_\psi [\langle \psi | G_\sigma | \psi \rangle])^2 \leq (\text{Tr}[G_\sigma])^2 \frac{\text{Tr}[\rho_\sigma^2]}{d^2}, \quad (\text{D9})$$

respectively. Here, $\|O\| := \sqrt{\max_{|v\rangle} \frac{\langle v | O^\dagger O | v \rangle}{\langle v | v \rangle}}$ is the spectral norm with $|v\rangle$ being the eigenstate of $O^\dagger O$.

Our objective now is to assess $\mathbb{E}_\psi [\langle O \rangle^{(\text{est})}] = \mathbb{E}_\psi [f/g]$ and its variance. One might initially consider the expansion

$$\mathbb{E}_\psi \left[\frac{f}{g} \right] = \mathbb{E}_\psi \left[\left(\frac{\mathbb{E}_\psi [f]}{\mathbb{E}_\psi [g]} + \Delta f \right) \frac{1}{1 + \Delta g} \right] = \frac{\mathbb{E}_\psi [f]}{\mathbb{E}_\psi [g]} \mathbb{E}_\psi \left[\left(\frac{\mathbb{E}_\psi [f]}{\mathbb{E}_\psi [g]} + \Delta f \right) (1 + \Delta g + \mathcal{O}(\Delta g^2)) \right], \quad (\text{D10})$$

assuming that $\Delta f := (f - \mathbb{E}_\psi [f])/\mathbb{E}_\psi [g]$ and $\Delta g := (g - \mathbb{E}_\psi [g])/\mathbb{E}_\psi [g]$ are small. However, this expansion is not convergent because $|\Delta g|$ can be larger than 1. To circumvent the issue, we partition the ensemble of $|\psi\rangle$ (2-design) into a subset Δ with a small positive number δ , where $|\Delta g|$ is small, and its complement $\bar{\Delta}$:

$$\Delta := \{|\psi\rangle \mid |\Delta f| \leq \delta \text{ and } |\Delta g| \leq \delta\}, \quad \bar{\Delta} := \{|\psi\rangle \mid |\Delta f| > \delta \text{ or } |\Delta g| > \delta\}. \quad (\text{D11})$$

Two important observations are that one can safely use expansions in terms of Δg in the subset Δ , and that the probability of $|\psi\rangle$ falling into $\bar{\Delta}$ is very small. The latter observation is supported by the Chebyshev inequalities

$$\Pr [|\Delta f| > \delta] < \frac{\text{Var}_\psi [f]}{\delta^2 (\mathbb{E}_\psi [g])^2} \leq \|O\|^2 \frac{\text{Tr}[\rho_\sigma^2]}{\delta^2}, \quad \Pr [|\Delta g| > \delta] < \frac{\text{Var}_\psi [g]}{\delta^2 (\mathbb{E}_\psi [g])^2} \leq \frac{\text{Tr}[\rho_\sigma^2]}{\delta^2}, \quad (\text{D12})$$

leading to

$$\Pr[\Delta] \geq 1 - (1 + \|O\|^2) \frac{\text{Tr}[\rho_\sigma^2]}{\delta^2}, \quad \Pr[\bar{\Delta}] < (1 + \|O\|^2) \frac{\text{Tr}[\rho_\sigma^2]}{\delta^2}, \quad (\text{D13})$$

where $\Pr[\Delta] + \Pr[\bar{\Delta}] = 1$. We ascertain that $\Pr[\bar{\Delta}]$ is indeed small because the purity $\text{Tr}[\rho_\sigma^2]$ diminishes exponentially with the system size N , as elaborated later in Eq. (D23). The inequalities in Eq. (D13) will be used repeatedly to bound the bias and variance in the subsequent analysis.

Bounding bias

Noticing that $\langle O \rangle = \mathbb{E}_\psi[f]/\mathbb{E}_\psi[g]$, we first establish the upper bound for the bias:

$$\begin{aligned} |\mathbb{E}_\psi[\langle O \rangle^{(\text{est})}] - \langle O \rangle| &= \Pr[\Delta] \left| \mathbb{E}_{\psi_\Delta} \left[\frac{f}{g} - \frac{\mathbb{E}_\psi[f]}{\mathbb{E}_\psi[g]} \right] \right| + \Pr[\bar{\Delta}] \left| \mathbb{E}_{\psi_{\bar{\Delta}}} \left[\frac{f}{g} - \frac{\mathbb{E}_\psi[f]}{\mathbb{E}_\psi[g]} \right] \right| \\ &\leq \left| \mathbb{E}_{\psi_\Delta} \left[\frac{f}{g} - \frac{\mathbb{E}_\psi[f]}{\mathbb{E}_\psi[g]} \right] \right| + \frac{(1 + \|O\|^2)\text{Tr}[\rho_\sigma^2]}{\delta^2} 2\|O\|, \end{aligned} \quad (\text{D14})$$

where $\mathbb{E}_{\psi_\Delta}[\cdot]$ represents the average of $|\psi\rangle$ over the subset of a state 2-design in Eq. (D11) and $\mathbb{E}_{\psi_{\bar{\Delta}}}[\cdot]$ is defined analogously. In deriving the inequality, we used the bound $|f/g - \mathbb{E}_\psi[f]/\mathbb{E}_\psi[g]| \leq 2\|O\|$. The first term is further bounded as

$$\left| \mathbb{E}_{\psi_\Delta} \left[\frac{f}{g} - \frac{\mathbb{E}_\psi[f]}{\mathbb{E}_\psi[g]} \right] \right| = \left| \mathbb{E}_{\psi_\Delta} \left[\left(\frac{\mathbb{E}_\psi[f]}{\mathbb{E}_\psi[g]} + \Delta f \right) \left(1 - \frac{\Delta g}{1 + \Delta g} \right) - \frac{\mathbb{E}_\psi[f]}{\mathbb{E}_\psi[g]} \right] \right| \leq \delta \left(1 + \frac{\|O\| + \delta}{1 - \delta} \right), \quad (\text{D15})$$

where the following was applied:

$$\left| \frac{\Delta g}{1 + \Delta g} \right| \leq \frac{\delta}{1 - \delta} \quad (\text{D16})$$

for $|\Delta g| \leq \delta \leq 1$. By substituting the bound from Eq. (D15) into the bias given in Eq. (D14), we derive

$$|\mathbb{E}_\psi[\langle O \rangle^{(\text{est})}] - \langle O \rangle| = \left| \mathbb{E}_\psi \left[\frac{f}{g} \right] - \frac{\mathbb{E}_\psi[f]}{\mathbb{E}_\psi[g]} \right| \leq \delta \left(1 + \frac{\|O\| + \delta}{1 - \delta} \right) + \frac{2\|O\|(1 + \|O\|^2)\text{Tr}[\rho_\sigma^2]}{\delta^2}. \quad (\text{D17})$$

Setting $\delta = (\text{Tr}[\rho_\sigma^2])^{1/3}/2$, we finally establish the following bound on the bias:

$$|\mathbb{E}_\psi[\langle O \rangle^{(\text{est})}] - \langle O \rangle| \leq (\text{Tr}[\rho_\sigma^2])^{1/3} (1 + 9\|O\| + 8\|O\|^3), \quad (\text{D18})$$

where we used the condition that $0 < \delta \leq 1/2$. As we will show later in Eq. (D23), the purity $\text{Tr}[\rho_\sigma^2]$ is exponentially small in the system size N .

Bounding variance

Using the same strategy, we bound the variance, which is the second term on the right-hand side of Eq. (D5), as follows:

$$\begin{aligned} \text{Var}_\psi[\langle O \rangle^{(\text{est})}] &= \mathbb{E}_\psi \left[\left(\frac{f}{g} - \mathbb{E}_\psi \left[\frac{f}{g} \right] \right)^2 \right] \\ &= \Pr[\Delta] \mathbb{E}_{\psi_\Delta} \left[\frac{f^2}{g^2} \right] + \Pr[\bar{\Delta}] \mathbb{E}_{\psi_{\bar{\Delta}}} \left[\frac{f^2}{g^2} \right] - \left(\Pr[\Delta] \mathbb{E}_{\psi_\Delta} \left[\frac{f}{g} \right] + \Pr[\bar{\Delta}] \mathbb{E}_{\psi_{\bar{\Delta}}} \left[\frac{f}{g} \right] \right)^2 \\ &\leq \Pr[\Delta] \mathbb{E}_{\psi_\Delta} \left[\frac{f^2}{g^2} \right] - \left(\Pr[\Delta] \mathbb{E}_{\psi_\Delta} \left[\frac{f}{g} \right] \right)^2 + \Pr[\bar{\Delta}] \cdot 3\|O\|^2 \\ &\leq \left(\mathbb{E}_{\psi_\Delta} \left[\frac{f^2}{g^2} \right] - \left(\mathbb{E}_{\psi_\Delta} \left[\frac{f}{g} \right] \right)^2 \right) + \Pr[\bar{\Delta}] \cdot 4\|O\|^2. \end{aligned} \quad (\text{D19})$$

The first term in the last equation is expanded as

$$\begin{aligned} &\mathbb{E}_{\psi_\Delta} \left[\frac{f^2}{g^2} \right] - \left(\mathbb{E}_{\psi_\Delta} \left[\frac{f}{g} \right] \right)^2 \\ &= \mathbb{E}_{\psi_\Delta} \left[\left(\frac{\mathbb{E}_\psi[f]}{\mathbb{E}_\psi[g]} + \Delta f - \frac{\mathbb{E}_\psi[f]}{\mathbb{E}_\psi[g]} \frac{\Delta g}{1 + \Delta g} - \frac{\Delta f \Delta g}{1 + \Delta g} \right)^2 \right] - \left(\mathbb{E}_{\psi_\Delta} \left[\frac{\mathbb{E}_\psi[f]}{\mathbb{E}_\psi[g]} + \Delta f - \frac{\mathbb{E}_\psi[f]}{\mathbb{E}_\psi[g]} \frac{\Delta g}{1 + \Delta g} - \frac{\Delta f \Delta g}{1 + \Delta g} \right] \right)^2 \\ &= \mathbb{E}_{\psi_\Delta} \left[\Delta f^2 + \frac{\mathbb{E}_\psi[f]^2}{\mathbb{E}_\psi[g]^2} \left(\frac{\Delta g}{1 + \Delta g} \right)^2 - 2 \frac{\mathbb{E}_\psi[f]}{\mathbb{E}_\psi[g]} \frac{\Delta f \Delta g}{1 + \Delta g} \right] \\ &\quad - \left(\mathbb{E}_{\psi_\Delta}[\Delta f]^2 + \frac{\mathbb{E}_\psi[f]^2}{\mathbb{E}_\psi[g]^2} \mathbb{E}_{\psi_\Delta} \left[\frac{\Delta g}{1 + \Delta g} \right]^2 - 2 \frac{\mathbb{E}_\psi[f]}{\mathbb{E}_\psi[g]} \mathbb{E}_{\psi_\Delta}[\Delta f] \mathbb{E}_{\psi_\Delta} \left[\frac{\Delta g}{1 + \Delta g} \right] \right) + \mathcal{O}(\delta^3) \\ &\leq \delta^2 + \|O\|^2 \frac{\delta^2}{(1 - \delta)^2} + 4\|O\| \frac{\delta^2}{1 - \delta} + \mathcal{O}(\delta^3). \end{aligned} \quad (\text{D20})$$

Thus, the upper bound of the variance in Eq. (D19) is obtained as

$$\text{Var}_\psi[\langle O \rangle^{(\text{est})}] \leq \delta^2 \left(1 + \frac{\|O\|^2}{(1-\delta)^2} + \frac{4\|O\|}{1-\delta} \right) + \frac{4(1+\|O^2\|)\|O\|^2 \text{Tr}[\rho_\sigma^2]}{\delta^2} + \mathcal{O}(\delta^3). \quad (\text{D21})$$

Setting $\delta = (\text{Tr}[\rho_\sigma^2])^{1/4}/2$, we find the bound

$$\text{Var}_\psi[\langle O \rangle^{(\text{est})}] \leq (\text{Tr}[\rho_\sigma^2])^{1/2} \left(\frac{1}{4} + 2\|O\| + 17\|O\|^2 + 4\|O\|^4 \right) + \mathcal{O}((\text{Tr}[\rho_\sigma^2])^{3/4}). \quad (\text{D22})$$

Scaling of purity

Let us evaluate the scaling of the purity $\text{Tr}[\rho_\sigma^2]$ as follows:

$$\text{Tr}[\rho_\sigma^2] = \frac{\text{Tr}[G_\sigma(E)^2]}{(\text{Tr}[G_\sigma(E)])^2} = \frac{\text{Tr}[G_{\sigma/\sqrt{2}}(E)]}{(\text{Tr}[G_\sigma(E)])^2} = e^{S_{\sigma/\sqrt{2}} - 2S_\sigma} = \mathcal{O}(e^{-\alpha N}), \quad (\text{D23})$$

where α is a positive constant independent of N . Here, we used that the entropy S_σ defined in Eq. (D2) is an extensive quantity, $S_\sigma = \Theta(N)$, and monotonically increases with σ , i.e.,

$$\frac{\partial S_\sigma}{\partial \sigma} = \frac{1}{\sigma^3} \frac{\text{Tr}[(E - \mathcal{H})^2 G_\sigma(E)]}{\text{Tr}[G_\sigma(E)]} \geq 0, \quad (\text{D24})$$

as shown in Ref. [55].

Success probability

Substituting the bounds from Eqs. (D18) and (D22) into the mean-square error in Eq. (D5), we obtain

$$\mathbb{E}_\psi[|\langle O \rangle^{(\text{est})} - \langle O \rangle|^2] \leq (\text{Tr}[\rho_\sigma^2])^{1/2} \left(\frac{1}{4} + 2\|O\| + 17\|O\|^2 + 4\|O\|^4 \right) + \mathcal{O}((\text{Tr}[\rho_\sigma^2])^{2/3}) \quad (\text{D25})$$

Note that the bound on the squared bias in Eq. (D18) is subleading relative to that on the variance in Eq. (D22).

Applying the Chebyshev inequality, we can bound the success probability as follows:

$$\Pr_{|\psi\rangle} \left[|\langle O \rangle^{(\text{est})} - \langle O \rangle| \leq \epsilon \right] \geq 1 - \frac{\mathbb{E}_\psi[|\langle O \rangle^{(\text{est})} - \langle O \rangle|^2]}{\epsilon^2} \geq 1 - \mathcal{O}\left(\frac{e^{-\alpha N/2}}{\epsilon^2}\right), \quad (\text{D26})$$

as stated in Eq. (13). Thus, we conclude that $\langle O \rangle^{(\text{est})}$ provides an ϵ -precise estimator of the microcanonical expectation value of O with high probability.

Appendix E: Resources for imaginary time evolution

We approximate the integral form of $G_\sigma(E)$ [55, 72]

$$G_\sigma(E) = \frac{\sigma}{\sqrt{2\pi}} \int_{-\infty}^{\infty} dt e^{-\frac{\sigma^2 t^2}{2}} e^{-i(E-\mathcal{H})t} \quad (\text{E1})$$

by truncating and discretizing the integral as

$$\tilde{G}'_\sigma(E) = \frac{\sigma}{\sqrt{2\pi}} \sum_{s=-S}^S \Delta t e^{-\frac{\sigma^2 (s\Delta t)^2}{2}} e^{-i(E-\mathcal{H})s\Delta t}. \quad (\text{E2})$$

We restate two useful results from Ref [72] for our analysis. Lemma 1 of Ref. [72] states that there exist parameters

$$S = \Theta\left(\frac{\|E - \mathcal{H}\|}{\sigma} \log \frac{1}{\epsilon'}\right), \quad \Delta t = \Theta\left(\frac{1}{\|E - \mathcal{H}\| \sqrt{\log \frac{1}{\epsilon'}}}\right), \quad (\text{E3})$$

such that

$$\|\tilde{G}'_\sigma(E) - G_\sigma(E)\| \leq \frac{\epsilon'}{2}. \quad (\text{E4})$$

The filter $\tilde{G}'_\sigma(E)$ is an approximation to $G_\sigma(E)$ provided that $e^{-iHs\Delta t}$ is treated exactly. Furthermore, Corollary 1 of Ref. [72] states that under an approximate implementation $U_s(\mathcal{H})$ of $e^{-iHs\Delta t}$,

$$\|U_s(\mathcal{H}) - e^{-iHs\Delta t}\| \leq \frac{\epsilon'}{4} \quad (\text{E5})$$

for all $s \in [-S, S]$. Consequently, the approximate filter operator

$$\tilde{G}_\sigma(E) = \frac{\sigma}{\sqrt{2\pi}} \sum_{s=-S}^S \Delta t e^{-\frac{\sigma^2(s\Delta t)^2}{2}} U_s(\mathcal{H}) \quad (\text{E6})$$

has an error upper-bounded by

$$\|\tilde{G}_\sigma(E) - G_\sigma(E)\| \leq \epsilon'. \quad (\text{E7})$$

From Eq. (E7), one can show

$$|\langle \psi_0 | O\tilde{G}_\sigma | \psi_0 \rangle - \langle \psi_0 | OG_\sigma | \psi_0 \rangle| = |\langle \psi_0 | O(\tilde{G}_\sigma - G_\sigma) | \psi_0 \rangle| \leq \|O\| \|\tilde{G}_\sigma - G_\sigma\| \leq \epsilon' \|O\|, \quad (\text{E8})$$

where $|\psi_0\rangle$ is an arbitrary quantum state. Recall that for positive real values $a, \tilde{a}, b, \tilde{b}$ satisfying $|\tilde{a} - a| \leq \epsilon' \|O\|$ and $|\tilde{b} - b| \leq \epsilon'$, the following inequality holds:

$$\left| \frac{\tilde{a}}{\tilde{b}} - \frac{a}{b} \right| \leq \frac{|a - \tilde{a}| \tilde{b}}{\tilde{b} b} + \frac{\tilde{a} |b - \tilde{b}|}{\tilde{b} b} \leq \frac{(\tilde{a} + \|O\| \tilde{b}) \epsilon'}{\tilde{b} b}. \quad (\text{E9})$$

Setting

$$a = \langle \psi_0 | OG_\sigma | \psi_0 \rangle, \quad \tilde{a} = \langle \psi_0 | O\tilde{G}_\sigma | \psi_0 \rangle, \quad b = \langle \psi_0 | G_\sigma | \psi_0 \rangle, \quad \tilde{b} = \langle \psi_0 | \tilde{G}_\sigma | \psi_0 \rangle, \quad (\text{E10})$$

we find

$$\left| \frac{\langle \psi_0 | O\tilde{G}_\sigma | \psi_0 \rangle}{\langle \psi_0 | \tilde{G}_\sigma | \psi_0 \rangle} - \frac{\langle \psi_0 | OG_\sigma | \psi_0 \rangle}{\langle \psi_0 | G_\sigma | \psi_0 \rangle} \right| \leq \frac{\epsilon' \|O\| (\langle \psi_0 | \tilde{G}_\sigma | \psi_0 \rangle + \langle \psi_0 | G_\sigma | \psi_0 \rangle)}{\langle \psi_0 | G_\sigma | \psi_0 \rangle \langle \psi_0 | \tilde{G}_\sigma | \psi_0 \rangle} \stackrel{\text{w.h.p.}}{\leq} \frac{\epsilon' \|O\|}{\text{Tr}[G_\sigma]/2^N} =: \epsilon, \quad (\text{E11})$$

where the second inequality holds with high probability. Here, we have defined $\epsilon = \epsilon' 2^N \|O\| / \text{Tr}[G_\sigma] = \epsilon' 2^N \|O\| / e^{S\sigma}$ using Eq. (D2).

Finally, we estimate the number of shots required to estimate $\langle \psi_0 | O\tilde{G}_\sigma | \psi_0 \rangle$ with the statistical uncertainty ϵ' . The variance of $\langle \psi_0 | OU_s | \psi_0 \rangle$ is given by

$$\begin{aligned} \text{Var}_{\text{shots}} [\langle \psi_0 | OU_s | \psi_0 \rangle] &:= \langle \psi_0 | (OU_s)^\dagger (OU_s) | \psi_0 \rangle - |\langle \psi_0 | OU_s | \psi_0 \rangle|^2 \\ &\leq \langle \psi_0 | U_s^\dagger O^\dagger OU_s | \psi_0 \rangle \leq \|O\|^2. \end{aligned} \quad (\text{E12})$$

Then, the variance of $\langle \psi_0 | O\tilde{G}_\sigma | \psi_0 \rangle$, where \tilde{G}_σ is given in Eq. (E6), is calculated as

$$\frac{\sigma^2}{2\pi} \sum_{s=-S}^S (\Delta t)^2 e^{-\sigma^2(s\Delta t)^2} \text{Var}_{\text{shots}} [\langle \psi_0 | OU_s | \psi_0 \rangle] \leq O(\sigma \Delta t \|O\|^2). \quad (\text{E13})$$

Refer to Eq. (E3) for Δt . To achieve a standard deviation of $O(\epsilon') = O(\epsilon e^{S\sigma} / (2^N \|O\|))$, the number of shots required is

$$N_{\text{shots}} = O\left(\frac{\sigma \Delta t \|O\|^2}{\epsilon'^2}\right) \approx O\left(\frac{\|O\|^4 2^{2N}}{\epsilon'^2 e^{2S\sigma}}\right), \quad (\text{E14})$$

where polynomial dependence on N is ignored in the approximate equality.

Appendix F: Additional experimental data for thermal expectation values

In this appendix, we present additional experimental results of the amplitudes $\mathcal{L}(t)$ and $\mathcal{L}_{Z_1 Z_2}(t)$, which complement those shown in Fig. 9, and are also obtained using the Quantinuum H1-2 system. The experimental setup is described in Sec. IV C.

First, we briefly outline an error mitigation scheme based on the depolarizing noise. We evaluate the mitigated value $\mathcal{L}_O(t)^{(\text{mit})}$ by renormalizing the experimentally obtained amplitude $\mathcal{L}_O(t)^{(\text{noisy})}$ as follows:

$$\mathcal{L}_O(t)^{(\text{mit})} = \frac{\mathcal{L}_O(t)^{(\text{noisy})}}{[1 - p_{2Q}^{(\text{ent})}(\mathcal{J}t/2)]^{N_{2Q}}}. \quad (\text{F1})$$

Here, O represents either the identity or the operator $Z_1 Z_2$, and $p_{2Q}^{(\text{ent})}(\theta) = \frac{5}{4} p_{2Q}(\theta)$ is the entanglement infidelity [85, 86, 100, 101] with N_{2Q} denoting the number of two-qubit gates involved in the controlled $\mathcal{O}\mathcal{U}(t)$ gate (see Fig. 8). The average two-qubit gate error rate $p_{2Q}(\mathcal{J}t/2)$ is given in Eq. (21). Specifically, in our experiments, $N_{2Q} = 112$ for the controlled $\mathcal{U}(t)$ gate and $N_{2Q} = 114$ for the controlled $Z_1 Z_2 \mathcal{U}(t)$ gate.

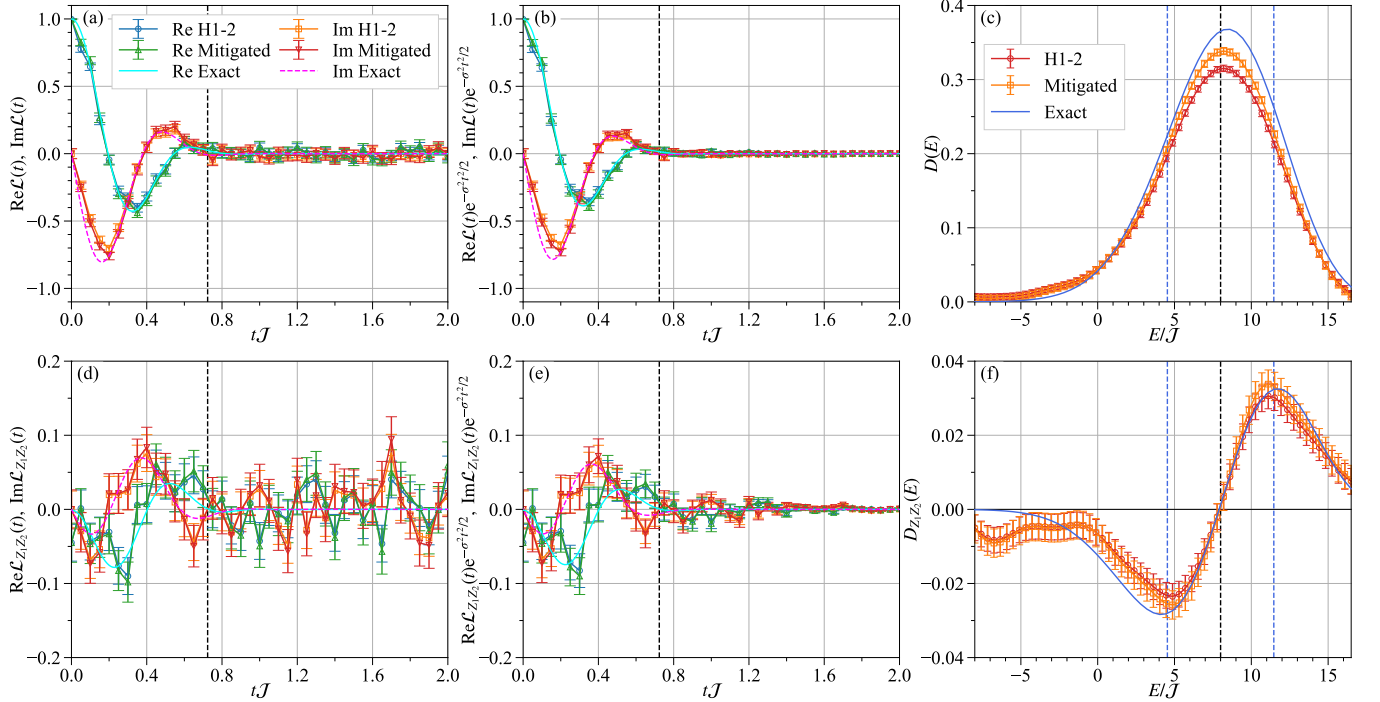


FIG. 17. (a) Real and imaginary parts of the Loschmidt amplitude $\mathcal{L}(t)$ for the one-dimensional Heisenberg model \mathcal{H}_{XX} with $N = 16$ sites under periodic boundary conditions. The experimental results $\mathcal{L}_O(t)^{(\text{noisy})}$ are obtained for the Floquet scrambled states $|\psi(m)\rangle$ with $m = 8$ and 16 using the Quantinuum H1-2 system. The error-mitigated results $\mathcal{L}_O(t)^{(\text{mit})}$ are obtained by renormalizing the experimental values as in Eq. (F1). The vertical line indicates $t = \sigma^{-1}$, where σ is defined in Eq. (28). For comparison, the ideal values obtained from classical calculations are also shown by solid and dashed curves for the real and imaginary parts, respectively. (b) Same as (a) but with the Loschmidt amplitude multiplied by the Gaussian weight $e^{-\sigma^2 t^2/2}$. (c) The associated density of states $D(E)$ obtained via Eq. (19) as a Fourier transform of the Gaussian-weighted Loschmidt amplitude $\mathcal{L}(t)e^{-\sigma^2 t^2/2}$ shown in (b). The black dashed vertical line indicates $E = E_\infty = 8\mathcal{J}$, and the blue dashed vertical lines indicate $E = E_\infty \pm \sigma_{\mathcal{H}} = 8\mathcal{J} \pm 2\sqrt{3}\mathcal{J}$, where $\sigma_{\mathcal{H}}$ is defined in Eq. (29). The ideal values obtained from classical calculations are also shown by a blue solid curve. (d-f) Same as (a-c) but for $\mathcal{L}_{Z_1 Z_2}(t)$ and $D_{Z_1 Z_2}(E)$. Note that the unmitigated results in (a) and (c) are the same as those shown in Figs. 9(a) and 9(b), respectively.

Figures 17(a,d) show the amplitudes $\mathcal{L}(t)$ and $\mathcal{L}_{Z_1 Z_2}(t)$ with and without the error mitigation, along with the corresponding ideal values obtained from classical calculations. While the difference is subtle, we observe that the error-mitigated $\mathcal{L}(t)^{(\text{mit})}$ tends towards the ideal value, particularly at early times $t \lesssim \sigma^{-1}$, where σ is defined in Eq. (28). In contrast, the error-mitigated $\mathcal{L}_{Z_1 Z_2}(t)^{(\text{mit})}$ is practically indistinguishable from the unmitigated counterpart $\mathcal{L}_{Z_1 Z_2}(t)^{(\text{noisy})}$ within the statistical errors due to the shot noise. This is because, at early times $t \lesssim \sigma^{-1}$, the signal of $\mathcal{L}_{Z_1 Z_2}(t)$ is nearly ten times smaller than that of $\mathcal{L}(t)$, implying that 100 times more shots are required to observe the difference, which is impractical.

Figures 17(b,e) show the amplitudes multiplied by the Gaussian weight $e^{-\sigma^2 t^2/2}$, i.e., $\mathcal{L}(t)e^{-\sigma^2 t^2/2}$ and $\mathcal{L}_{Z_1 Z_2}(t)e^{-\sigma^2 t^2/2}$, respectively. The Gaussian factor $e^{-\sigma^2 t^2/2}$ in Eq. (15) attenuates these amplitudes and their statistical fluctuations for $t \gtrsim \sigma$. This

illustrates that only the amplitudes at early times $t \lesssim \sigma$ significantly contribute to the associated density of states in Eqs. (18) and (19).

Figures 17(c,f) show $D(E)$ and $D_{Z_1 Z_2}(E)$, respectively. Although the difference in the the Loschmidt amplitude $\mathcal{L}(t)$ with and without the error mitigation, as shown in Fig. 17(a), is small, the error mitigated $D(E)$ shows better agreement with the ideal results compared to the unmitigated one. However, as expected, no significant improvement beyond the statistical errors is observed in $D_{Z_1 Z_2}(E)$ due to the small signals of $\mathcal{L}_{Z_1 Z_2}(t)$ relative to the statistical errors. Despite the small signals of $\mathcal{L}_{Z_1 Z_2}(t)$, as discussed for $\langle Z_1 Z_2 \rangle^{(\text{est})}$ in Sec. IV C, we observe excellent agreement with the ideal results within the statistical uncertainty in the energy range $E_\infty - \sigma_{\mathcal{H}} \lesssim E \lesssim E_\infty + \sigma_{\mathcal{H}}$ due to the concentrated energy spectrum around E_∞ . Here, $\sigma_{\mathcal{H}}$ is defined in Eq. (29). The experimental data of $D_{Z_1 Z_2}(E)$ indeed changes its sign such that $D_{Z_1 Z_2}(E) < 0$ for $E \lesssim E_\infty$ and $D_{Z_1 Z_2}(E) > 0$ for $E \gtrsim E_\infty$, as theoretically expected.

Importantly, the effect of depolarizing noise mostly cancels out between the numerator and denominator in the thermal expectation value $\langle Z_1 Z_2 \rangle^{(\text{est})} = D_{Z_1 Z_2}(E)/D(E)$, as generally given in Eq. (20), similarly to the normalized OTOC in Eq. (A6). We expect that this error mitigation scheme is effective even for more complex observables O where N_{2O} in $\mathcal{L}_O(t)$ is significantly larger than that of $\mathcal{L}(t)$, including higher-weight Pauli strings and dynamical correlation functions.